Invited paper

OPTO-ELECTRONICS REVIEW 7(3), 153–180 (1999)

GaAs homojunction interfacial workfunction internal photoemission (HIWIP) far-infrared detectors

A.G.U. PERERA* and W.Z. SHEN

Department of Physics and Astronomy, Georgia State University
Atlanta, 30303 Georgia, USA

The recent development of p-GaAs homojunction interfacial workfunction internal photoemission (HIWIP) far-infrared (> 40 μm) detectors is reviewed, both theoretically and experimentally. The emphasis is on the detector photoresponse mechanism and detector performance, which include doping concentration dependence of workfunction, far-infrared free carrier absorption, internal photoemission, interfacial barrier collection, and detector dark current, responsivity, quantum efficiency, bias effect, cutoff wavelength, uniformity, crosstalk, photoconductive gain, response time and noise. Promising results indicate that p-GaAs HIWIP detectors have great potential to become a strong competitor in far-infrared applications.

Keywords: p-GaAs homojunction interfacial workfunction internal photoemission far-infrared detectors, extended cutoff wavelength, emitter layer concentration effect, photoresponse mechanism

1. Introduction

High performance far infrared (40~200 μm) semiconductor detectors as well as large focal plane arrays are required for space astronomy applications [1], such as NASA's Stratospheric Observatory for Infrared Astronomy (SOFIA), airborne mission, Next Generation Space Telescope (NGST), and the ESA's Far-infrared and Sub-mm Telescope (FIRST) programs, for studying interacting galaxies, star formation and composition, and interstellar clouds. The conventional detectors used for the far-infrared range are extrinsic Ge photoconductors, such as unstressed Ge:Ga devices for the 40–120 μm and stressed Ge:Ga for the 120–200 μm [2], Ge blocked-impurity-band (BIB) detectors [3,4], and GaAs photoconductors [5] are also under development in order to overcome the limitations inherent in conventional extrinsic photoconductors and extend the cutoff wavelength λ_c. These space applications have placed stringent requirements on the performance of FIR detectors and arrays such as high detectivity, low dark current, high uniformity, radiation hardness, low power dissipation, and mature circuit intergrating technology. However, there are many technological challenges for fabricating larger format arrays in germanium [6]. At present, no Si FIR detectors exist that can operate effectively beyond 40 μm at low backgrounds [7].

The idea of internal photoemission detectors was first proposed by Shepherd et al. [8] in Schottky barrier structures. Due to the recent advances in epitaxial growth technology, up to now, several types of internal photoemission infrared detectors have been proposed and demonstrated [9]. Among them, one important type is metal-semiconductor Schottky barrier IR detectors, such as the highly developed PtSi/Si detector operating in 3–5 μm [10]. Another type is semiconductor heterojunction IR detectors, such as Ge_xSi_{1-x}/Si detectors [11,12] developed for 8–14 μm or even longer wavelengths. There is also a degenerate Si homojunction detector [13], which has a response in 1–7 μm. Since the structure of the latter detector is very similar to the detectors investigated in this work, below it is categorized as the type III detector. In these detectors, the absorber/photoemitter "electrode" may be a metal, a metal silicide or a degenerate semiconductor. Thus, following the terminology of Lin and Maserjian [11], all of these detectors can be described as HIP, i.e., hetero- (or homo-) junction internal photoemission detectors. The actual

* e-mail: uperera@gsu.edu

physical processes taking place in the emitter layer are still not well understood, although several theoretical models [14-18] have been developed to describe the hot carrier photoemission.

The concept of homojunction internal photoemission for FIR detection was first proposed and demonstrated on forward biased commercial Si p-i-n diodes at 4.2 K [19]. The detector λ_c was extended to very long wavelength range (> 200 μm), and similar results were also obtained for Ge and InGaAs p-i-n diodes [20]. In addition, experimental results obtained with a single p^+-i interface structure were reported, and the concept of multilayer structures was proposed [20]. Also, a somewhat similar detector concept was proposed and demonstrated for a Si MBE multilayer structure in the long-wave infrared (LWIR) range [22]. The detection mechanism [19] assumes that the biased interface structure, consisting of a heavily doped IR absorber layer and an intrinsic (or lightly doped) layer (n^+-i or p^+-i), can be depicted as an internal photoemitter at low temperatures (≤ 20 K). For an n^+-i (p^+-i) structure, the Fermi level in the heavily doped layer can lie below (above) the conduction (valence) band edge of the i-layer, giving rise to an interfacial workfunction, which defines the long wavelength IR cutoff for the detector. When the doping concentration is above the metal-insulator transition (Mott transition) value, the detector can be regarded as a metal photoemitter (type II detector), which was denoted as homojunction interfacial workfunction internal photoemission (HIWIP) FIR detectors [23], otherwise it can be regarded as a semiconductor photoemitter (type I detector). Following a linearly distributed space charge model [24], it was shown that the space charge effect at the interface is negligible at low temperatures. The initial experimental results were obtained on commercial p-i-n diodes [19-21], which were not designed for IR detectors, detector performance was not very high. In order to fabricate detectors with high performance, device parameters should be optimized. This in turn required a better understanding of the detector photoresponse mechanism, detailed modelling and experimental work.

The operation of HIWIP detectors is based on the internal photoemission occurring at the interface between a heavily doped absorber/emitter layer and an intrinsic layer, with the cutoff wavelength λ_c mainly determined by the interfacial workfunction Δ: λ_c (μm) = 1.24/Δ (eV). The detection mechanism of HIWIP detectors involves FIR absorption in the highly-doped thin emitter layers by free carrier absorption followed by the internal photoemission of photoexcited carriers across the junction barrier and then collection. Modelling studies [25,26] have shown that Si HIWIP FIR detectors could have a performance comparable to that of conventional Ge FIR photoconductors [27] or Ge BIB FIR detectors [28], with unique material advantages. Therefore, this novel detector approach provides considerable promise for developing FIR imaging devices, by taking advantage of a mature Si or GaAs material technology and a tailorable λ_c which covers several tens to a few hundreds of μm.

In addition to Si, significant effective band-gap shrinkage has also been observed for heavily doped p-GaAs [29]. Better carrier transport properties of GaAs, such as higher mobility will translate into a higher gain, which may produce improved performance for this type of detectors. Also, the recent rapid development of GaAs based long-wavelength quantum-well focal plane array cameras make GaAs another promising candidate for developing HIWIP FIR detectors. The progress of n-GaAs FIR photoconductors has been slow due to difficulties in growing high purity materials [27]. This paper reviews the recent development of Be-doped p-GaAs HIWIP FIR detectors.

This paper is arranged in the following way. In Sec. 2, three different types of HIP detectors are compared; and an estimate of the workfunction dependence on the doping concentration above the Mott transition is given. In Sec. 3, an analytical model is introduced to describe the spectral response in single layer (p^+-i) HIWIP detectors, which includes free carrier absorption, photoexcitation, emission to the interfacial barrier, hot carrier transport, and barrier collection. In Sec. 4, effect of emitter layer concentration on the performance of GaAs p^+-i HIWIP FIR detectors is presented. In Sec. 5, a high performance p-GaAs HIWIP FIR detector is demonstrated with the emphasis on its response, quantum efficiency, bias effect, uniformity, crosstalk, gain, response time, and noise. Some concluding remarks and discussions summarized in Sec. 6. Although the analysis in this paper is mainly for a p^+-i interface structure, similar results can be performed for an n^+-i structure with small modifications.

2. Three different types of HIP detectors and workfunction dependence of HIWIP detectors

The basic structure of HIP detectors consists of a heavily doped layer, which acts as the IR absorber region, and an intrinsic (or lightly doped) layer across which most of the external bias is dropped. According to the doping concentration level in the heavily doped layer, the HIP detectors can be divided into three

 © 1999 COSiW SEP, Warsaw

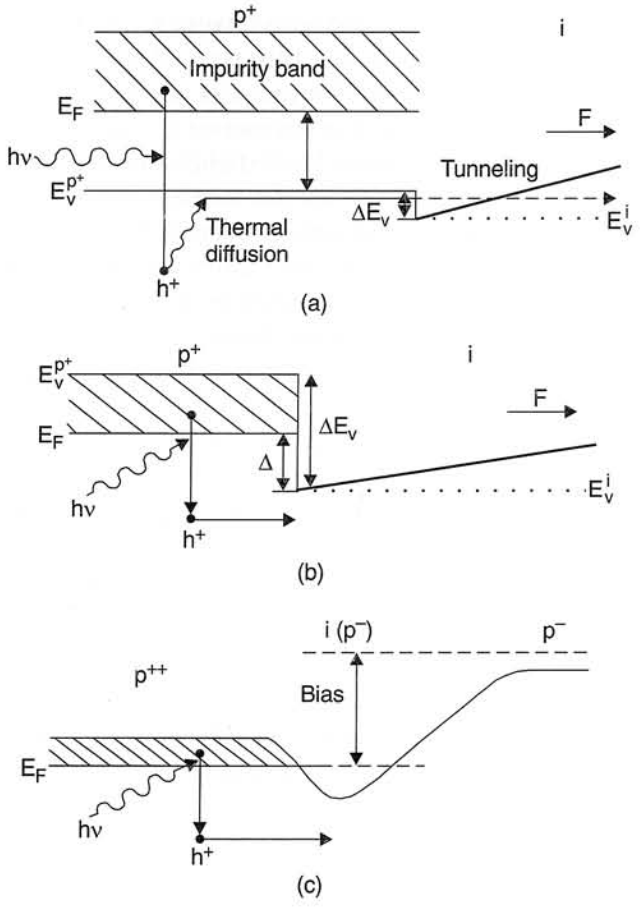

Fig. 1. Energy band diagrams for three different p types of HIP detectors. (a) Type I: $N_a < N_c (E_F > E_v^{p^+})$; (b) Type II: $N_c < N_a < N_0 (E_v^{p^+} > E_F > E_v^i)$, and (c) Type III: $N_a > N_0 (E_F < E_v^i)$. Here, N_c is the Mott's critical concentration and N_0 is the critical concentration corresponding to $\Delta = 0$. In (a) and (b), the valence band edge of the i-layer is represented by a dotted line for $V_b = V_0$ (flatband) and by a solid line for $V_b > V_0$.

types as shown in Figs. 1(a), 1(b), and 1(c), which show different photoresponse mechanisms and response wavelength ranges.

2.1. Type I HIP detectors: $N_a < N_c (E_F > E_c^{n^+})$

When the doping concentration N_a in the p^+-layer is high but below the Mott critical value N_c, an impurity band is formed. At low temperatures, the Fermi level is located in the impurity band. The incident FIR light is absorbed due to the impurity photo-ionization, with a workfunction given by $\Delta = E_F - E_v^{p^+}$, where $E_v^{p^+}$ is the valence band edge in the p^+-layer. An electric field is formed in the i-layer by an external bias to collect photoexcited electrons generated in the p^+-layer. Obviously, type I HIP detectors are analogous to semiconductor photoemissive detectors [30] in their operation, which can be described by a three-step process [see Fig. 1(a)]. (1) Holes are photoexcited from filled impurity band states above Fermi level into empty states below the valence band edge; (2) Photoexcited holes first rapidly thermalize into the top of the valence band by phonon relaxation and then diffuse to the emitting interface, with the transport probability determined by the hole diffusion length; (3) Those holes reaching the emitting interface tunnel through an interfacial barrier ΔE_v, which is due to the offset of the valence band edge caused by the band-gap narrowing effect, and are collected by the electric field in the i-region. The collection efficiency will depend on the tunneling probability which in turn depends on the i-region electric field. The λ_c can be tailorable with the doping concentration to some extent, because with the increase of doping concentration the impurity band broadens and its peak density of state moves rapidly towards the valence band [31].

In the above discussion, the impurity compensation in the p^+-layer, which is unavoidable for the actual heavily doped semiconductors, was neglected. Due to the compensation effect, electric field can be induced in the p^+-layer by the external bias. If the compensated acceptor concentration is very small, the electric field region may extend over a large part of the p^+-layer. This is just the case of blocked-impurity-band (BIB) detectors [32,33], for which the photoexcited hole collection mechanism is different from the processes (2) and (3) described in the above paragraph. In contrast to the type I HIP detector, the BIB detector resembles a reverse-biased photovoltaic detector in its operation, with the collection efficiency in the electric field region approaching 100%. However, if the compensated acceptor concentration is high, in the most part of the p^+-layer there is no electric field induced when an external voltage is applied, except for a very small depletion region near the p^+-i interface. In this case, the photoresponse mechanism still can be described by the processes developed above for type I HIP detectors. Usually, the quantum efficiency of a type I HIP detector is less than that of a BIB detector due to the nature of internal photoemission. However, when the doping concentration is so high that it is near the Mott transition, technologically it is less likely to get a very low compensated acceptor concentration. So, it is expected that the type I HIP detector still may have an advantage in a wavelength range longer than that of the BIB detector.

2.2. Type II HIP detector: $N_c < N_a < N_0 (E_v^{p^+} > E_F > E_v^i)$

When the doping concentration is above the Mott transition, the impurity band is linked with the valence band edge, and the p^+-layer becomes metallic. Even in this case, the Fermi level can still be above the valence band edge of the i-layer ($E_F > E_v^i$) due to the bandgap narrowing effect, giving rise to a workfunction $\Delta = E_F - E_v^i$ as shown in Fig. 1(b), unless N_a exceeds a critical concentration N_0 at which $\Delta = 0$. The workfunction dependence on doping concentration for this case will be discussed next. Type II HIWIP detectors are analogous to Schottky barrier IR detectors in their operation. One of their unique features is that in principle, there is no restriction on λ_c, which is tailorable, since the workfunction can become arbitrary small with increasing doping concentration. This means that the HIWIP FIR detectors with any λ_c can be developed as needed. Unlike type I HIP detectors, the photon absorption in type II HIWIP detectors is due to free carrier absorption. In spite of the fact that the free carrier absorption coefficient in the metallic p^+-layer is lower than in a metal due to the lower concentration, the type II HIWIP detector has a higher internal quantum efficiency than the Schottky barrier detector due to the reduction of the Fermi energy. In addition, the hot hole scattering length in HIWIP detectors could be larger than in metals due to the lower hole energy. The photoemission of photoexcited holes from the p^+-layer into the i-layer is determined by the emission to the interfacial barrier, hot hole transport and barrier collection process. The emission probability depends on the photon energy and the Fermi energy. The transport probability is governed by various elastic and inelastic hot hole scattering mechanisms occurring in the p^+-layer. The collection efficiency is due to the image force effect at the p^+-i interface, which gives rise to a voltage dependence of quantum efficiency. In next section, an analytic model will be presented to give the related formula for spectral response.

2.3. Type III HIP detector: $N_a > N_0 (E_F < E_v^i)$

When the doping concentration is so high that the Fermi level is below the valence band edge of the i-layer, the p^+-layer becomes degenerate, and a barrier associated with a space charge region is formed at the p^+-i interface due to the hole diffusion, as shown in Fig. 1(c). The barrier height depends on the doping concentration and the applied voltage, giving rise to an electrically tunable λ_c. This type of device was first demonstrated by Tohyama et al. [13] using a structure composed of a degenerate n^{++} hot carrier emitter, a depleted barrier layer (lightly doped p, n or i), and a lightly doped n-type hot carrier collector. As the bias voltage is increased, the barrier height is reduced, the spectral response shifts toward longer wavelength, and the signal increases at a given wavelength. The photoemission mechanism of type III HIP detectors is similar to that of type II HIWIP detectors, with the major difference in that they have different response wavelength ranges and different operating temperature ranges. The type II HIWIP detector is a FIR detector, and usually operates at temperatures much lower than 77 K. In contrast, the type III HIP detectors are expected to operate near 77 K and have responses in the mid-wave infrared (MWIR) and LWIR ranges [9].

2.4. Workfunction dependence on doping concentration above Mott transition

One of the key factors for the design of HIWIP detectors is to determine the doping concentration dependence of the interfacial workfunction (hence λ_c). The heavy doping effects on semiconductor properties, such as the bandgap narrowing, have been extensively studied, from both theoretical and experimental respects [31]. But the physical mechanism is not yet well understood. Also, there is little or no experimental data available describing the workfunction dependence on doping concentration above the Mott transition. Here a recently developed theoretical model is projected [34]. This would give simple but accurate closed form equations for band-gap narrowing to obtain an approximate relationship of λ_c vs doping concentration for the type II HIWIP FIR detectors to compare with our experimental results.

As the doping concentration increases, the impurity band broadens and becomes increasingly asymmetrical, and its peak moves towards the valence (conduction) band edge rapidly. At the same time, the valence (conduction) band edge also starts moving upwards (downwards) in the bandgap. At the Mott transition concentration, the impurity band and the valence (conduction) band merge with each other, and the semiconductor changes from a nonmetal to a metal (Mott transition). Above the Mott transition, with further increasing the doping concentration, the impurity band starts to shrink and finally becomes absorbed into the valence (conduction) band [31].

 © 1999 COSiW SEP, Warsaw

The lowering of the valence (conduction) band edge, ΔE_v (ΔE_c), can be described using the high--density theory. It has been shown [31] that this theory does describe the behavior of heavily doped Si and Ge to a fair degree of accuracy in the high-density regimes, i.e., above the Mott critical concentration, and gives reasonable results even at doping concentrations as low as 10^{18} cm^{-3}. The main result of this theory is that the hole-hole (electron-electron) interaction (many-body effect) causes a rigid upward (downward) shift of the valence (conduction) band, $\Delta E^{ex}_{v(c)}$, which is also known as exchange energy. The hole (electron)-impurity interaction causes an additional shift, $\Delta E^{i}_{v(c)}$, and also distorts the density of states function. In this theory, the semiconductor is assumed to be uncompensated and all impurities ionized so that the free carrier concentration is equal to the doping concentration N_a. In principle, this theory is valid close to 0 K.

Recently, Jain and Roulston [34] have derived a simple and accurate expression for the shift of the majority band edge, ΔE_{maj}, that can be used for all n- and p-type semiconductors and for any doping concentration in the high-density regime. By introducing two correction factors to take deviations from the ideal band structure into account, ΔE_{maj} can be expressed as

$$\Delta E_{maj} = \Delta E^{ex}_{maj} + \Delta E^{i}_{maj} \tag{1}$$

with

$$\Delta E^{ex}_{maj} = 1.83 \Lambda a \left(\frac{4\pi N_a}{3 N_m} \right)^{1/3} R$$
$$\Delta E^{i}_{maj} = \frac{1.57 a}{N_m} \left(\frac{4\pi a N_a}{3} \right)^{1/2} R \tag{2}$$

where N_a is the doping concentration, $R = 13.6 m_d/\varepsilon_s^2$ (eV) is the effective Rydberg energy, a = 0.53 ε_s/m_d (Å) is the effective Bohr radius, m_d is the effective density of state mass, and ε_s is the relative dielectric constant. The correction factor Λ takes into account the effect of anisotropy of the bands in n-type semiconductors and the effect of interactions between the light and heavy hole valence bands in p-type semiconductors. N_m is the number of conduction band minima in the case of n-type Si and n-type Ge, and $N_m = 2$ for all p-type semiconductors.

The modified expression for the Fermi energy to take the multiplicity of the majority band into account is given by [35]

$$E_F = \frac{\hbar^2 k_F^2}{2m^*} = \frac{\hbar^2}{2m_d} \left(\frac{3\pi^2 N_a}{N_m} \right)^{2/3}. \tag{3}$$

So, the workfunction is

$$\Delta = \Delta E_{maj} - E_F \tag{4}$$

The cutoff walength is given by λ_c (μm) = 1.24/Δ(eV).

Using above equations, the doping concentration dependence of ΔE_{maj}, E_F, Δ, and λ_c was calculated. The results for p-type GaAs are shown in Fig. 2. Similar calculations have also been performed for Si and Ge for both p- and n-types [23]. The critical concentrations N_0 which correspond to Δ = 0 can be obtained from the Δ vs N_a relationships. The Mott critical concentration N_c can be estimated by using the following approximate expression [36]

$$N_c^{1/3} a \sim \pi/12 \sim 0.25 \tag{5}$$

Table 1 shows the values of N_0 and N_c calculated for both n- and p-type Si, Ge, and GaAs, together with the parameters used in the calculation. As discussed in Sec. 2.2, the type II HIWIP detector can operate in the doping concentration range $N_c < N_a < N_0$. Although the actual critical concentrations depend on the impurity selected for doping, above calculations will give an estimate for the workfunction, which is important for the design of type II HIWIP detectors. It is seen from Fig. 2 that as N_a approaches N_0, λ_c becomes very sensitive to N_a, that is, only a small increase in N_a can cause a large increase λ_c. Furthermore, λ_c of the HIWIP detector can easily be tuned by the doping concentration to meet the requirements of up to 200 μm.

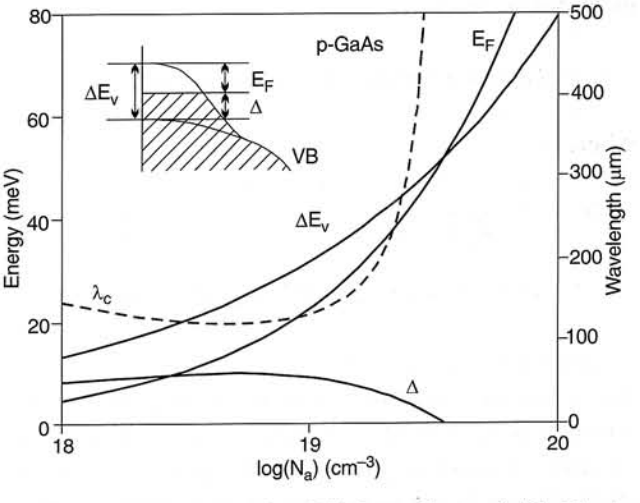

Fig. 2. Doping concentration (N_a) dependence of ΔE_v, E_F, Δ, λ_c, calculated using the high-density theory for p-type GaAs. The inset shows the shift of majority band edge and the position of Fermi level, with the shaded area representing the energy states filled by electrons.

Table 1. Parameters used for different semiconductors and calculated critical concentrations (N_c and N_0).

	n-Si	p-Si	n-Ge	p-Ge	n-GaAs	p-GaAs
ε_s	11.4	11.4	15.4	15.4	13.0	13.0
m_d	0.33	0.59	0.22	0.36	0.0665	0.47
N_m	6	2	4	2	1	2
Λ	1	0.75	0.84	0.75	1	0.75
R_H (meV)	34.5	61.7	12.6	20.6	5.4	38.1
a_H (Å)	18.3	10.2	37.1	22.7	103.6	14.6
N_c (cm^{-3})	2.55×10^{18}	1.47×10^{19}	3.06×10^{17}	1.34×10^{18}	1.41×10^{16}	5.02×10^{18}
N_0 (cm^{-3})	6.0×10^{19}	1.0×10^{20}	3.5×10^{18}	8.1×10^{18}	1.5×10^{17}	3.3×10^{19}

3. Theoretical model of spectral response

3.1. Photoexcitation

A single p^+-i (or n^+-i) structure consists of three layers (see Fig. 3): the heavily doped emitter layer, the intrinsic (or lightly doped) layer, and the bottom contact layer, with the thicknesses W_e, W_i and W_b, the doping concentrations N_e, N_i and N_b, and the absorption coefficients α_e, α_i and α_b, respectively. The photoexcited electrons generated in the bottom contact layer make no contribution to the photocurrent, hence the light flux I_0 should be incident normally from the top side to reduce the absorption in the bottom contact. The front and back reflectances are R_F and R_B respectively, whose variation with wavelength can be ignored. If the multiple internal reflection effect is considered, the generation rate of photoexcited electrons is given by

$$G(x) = G_1 \exp(-\alpha_e x) + G_2 \exp(\alpha_e x) \qquad (6)$$

where

$$G_1 = \frac{\alpha_e I_0 (1 - R_F)}{1 - R_F R_B \exp[-2(\alpha_e W_e + \alpha_i W_i + \alpha_b W_b)]}$$

$$G_2 = G_1 R_B \exp[-2(\alpha_e W_e + \alpha_i W_i + \alpha_b W_b)]$$

The FIR absorption in the i-layer can be neglected due to the fact that $\alpha_i W_i << \alpha_e W_e$, $\alpha_b W_b$. The photon absorption probability, defined as the ratio of the number of photoexcited carriers generated in the emitter layer to the number of incident photons, is

$$\eta_a = \int_0^{W_e} G(x)dx / I_0 = \frac{(1 - R_F)(1 + R_B \exp[-(\alpha_e W_e + 2\alpha_b W_b)])[1 - \exp(-\alpha_e W_e)]}{1 - R_F R_B \exp[-2(\alpha_e W_e + \alpha_b W_b)]} \qquad (7)$$

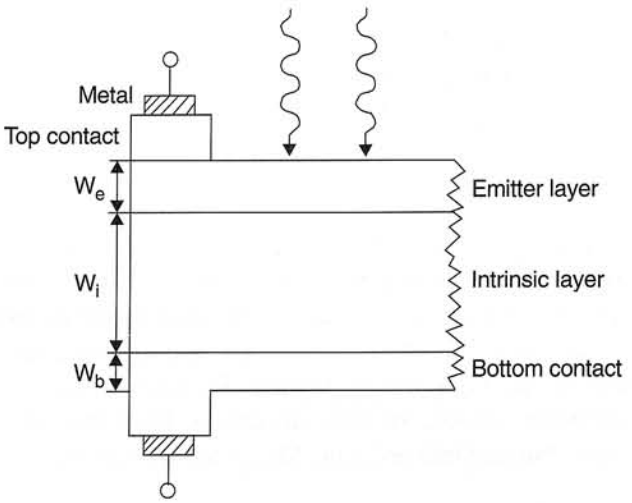

Fig. 3. Basic structure of frontside illuminated single type II HIP detector. In order to reduce the FIR absorption loss in the contact layers, the top (bottom) contact layer under (above) the metal plate can be formed as a ring surrounding the photosensitive area, and the bottom contact layer within the active area should be made as thin as possible. The absorption efficiency in the emitter layer can be increased by the multiple internal reflection.

One special case is that as ($\alpha_b W_b \to \infty$, $\eta_a \to (1 - R_F)$ $[1 - \exp(-\alpha_e W_e)]$. Another special case is that for $R_F \to 0$ and $R_B \to 1$ (by using antireflection coating and optical cavity), $\eta_a \to (1 + \exp[-(\alpha_e W_e + 2\alpha_b W_b)])$ $[1 - \exp(-\alpha_e W_e)]$. To reduce the effect of the bottom contact layer, α_b (by lowering N_b) and W_b should be decreased as far as possible.

3.2. Free carrier absorption

From the HIWIP detection mechanism, it is seen that the free carrier absorption plays a very important

 © 1999 COSiW SEP, Warsaw

role in the detector performance. It is important to understand the FIR free carrier absorption behaviour in heavily doped GaAs thin films, due to both fundamental and device performance reasons. Although the free carrier absorption in GaAs has been widely studied in the literature, this was limited to relatively short wavelengths (≤ 20 μm) [37]. Until recently, no free carrier absorption data were available for the wavelength range ≤ 50 μm, where the HIWIP FIR detectors usually work.

The transmission and reflection measurements for Be-doped MBE grown GaAs thin films were reported recently [38]. The absorption A in thin film is determined from the transmission T' and reflection R in conjunction with the expression

$$A = 1 - T' - R \tag{8}$$

and further subtraction of the absorption of the substrate. The thin film in that study was grown by the same MBE conditions as for the HIWIP detector samples. The epilayer thickness (d) of the absorption samples is 1000 Å with Be concentrations of 1×10^{18}, 5×10^{18}, and 2×10^{19} cm^{-3}. The absorption results of the thin film with a concentration of 2×10^{19} cm^{-3} over the wavelength range from 50 to 200 μm are shown in Fig. 4. The measured values of absorption were found to be almost independent of wavelength, which is similar to the cases of Schottky barrier IR detector

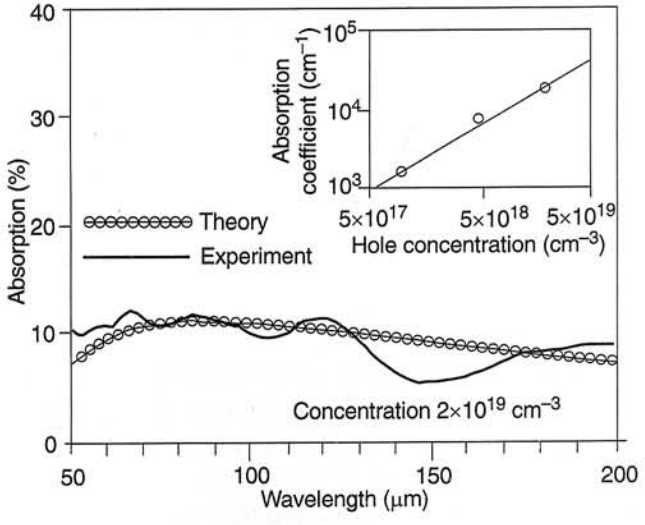

Fig. 4. Experimental FIR free carrier absorption in a p-GaAs thin film with the thickness of 1000 Å and doping concentration of 2×10^{19} cm^{-3} at room temperature (solid curve). The circles indicate the calculated results. The inset shows the experimental free hole absorption coefficient of three p-GaAs thin films at 80 μm (open circles) as a function of hole concentration at room temperature, together with its linear regression relation.

samples beyond the lattice bands [39] and GeSi layers above 15 μm [40]. Since free carrier absorption is an indirect transition process involving the light absorption and quasi-particle interaction (such as phonons, defects and lattice imperfections) by free carriers, the weak energy of photons in the FIR region results in a reduced excitation of carriers to higher energy levels within the same energy valley.

The theoretical absorption curve shown in Fig. 4 was calculated from the complex dielectric constant of the GaAs layer by matching electric and magnetic fields at the interfaces [41]. The dielectric constant of the thin film is derived from the frequency-dependent conductivity for free carriers by

$$\sigma = \frac{\sigma_0}{1 - i\omega\tau_{rt}} \tag{9}$$

where σ_0 is the dc conductivity and τ_{rt} is the relaxation time, which is independent of frequency ω in the semiclassical transport theory. Since the main interest is in the FIR range (≥ 50 μm), the other contributions, e.g., intervalence band transitions and lattice vibrations, were ignored. The carrier concentration is estimated from the doping level, while the relaxation time used was 1.7×10^{-14} s as measured for sample with similar doping levels [37]. This means that no free parameters are used to fit the experimental data with the modelling results. The reasonably good agreement between the experimental and theoretical results strongly demonstrates that the absorption is actually due to the contribution of free carriers. Further evidence for the identification of free carrier absorption in these thin films can be clearly seen from the absorption of their substrates, where the experiments show that their absorption can generally be neglected (the absorption coefficient is in the order of 10^{-2} cm^{-1}, in comparison with the order of $10^3 \sim 10^4$ cm^{-1} in thin films). The absorption coefficient α can be calculated by

$$a = \frac{1}{d}\ln\left(\frac{1-R}{T'}\right) \tag{10}$$

The relationship between the free hole absorption coefficient and the hole concentration, which is the most important result in connection with the HIWIP detectors, was also obtained. The strength of the free hole absorption at a wavelength of 80 μm is shown in the inset of Fig. 4. The absorption can be well described by a linear relation between the absorption coefficient and the concentration of holes, just as in the

case of Si thin films [42,43]. The fitted regression formula as a function of hole concentration P is found to be

$$\alpha = 8.28 \times 10^{-16}\ cm^2 \times P \tag{11}$$

The large value of the absorption coefficient in FIR range is suitable for the HIWIP detectors, since the absorption coefficient varies very little with temperature due to the almost invariant carrier concentration and mobility with temperature. Measurements also show that the free carrier absorption increases with increased doping concentration, which means highly doped emitter layers are more attractive for higher quantum efficiency in HIWIP detectors. This is expected as the free carrier absorption is proportional to both the carrier concentration and scattering rate (also increases with doping), and has been demonstrated in the experimental results in Sec. 4.5.

3.3. Internal quantum efficiency

The internal quantum efficiency η_i was obtained following a simplified Vickers-Mooney model [15,16] as

$$\eta_i = \frac{\eta_0}{1-\gamma+\gamma\eta_0/\eta_M} \tag{12}$$

where $\eta_M = N_M/N_T$ is the ratio of capturable carriers to photoexcited carriers and $\gamma = L_e/(L_e + L_p)$ is the probability that an excited carrier will collide with a phonon before it collides with a cold carrier. The inelastic scattering with cold carriers, which is assumed to "cool" the excited carriers to below the barrier energy, is characterized by the scattering length L_e; elastic scattering with phonons and impurities is characterized by the scattering length L_p. The fraction of carriers captured prior to any bulk scattering events (e-e or e-p) is given by [16]

$$\eta_0 = \frac{L^*}{W_e} U(W_d/L^*)\eta_{id} \tag{13}$$

with $L^* = 1/L_e + 1/L_p$ and η_{id} being the ideal internal quantum efficiency describe using an escape cone model [44] and $U(W_e/L^*) \sim [1 - \exp(-W_e/L^*)]^{1/2}$.

3.4. Barrier collection

A strong bias dependence of spectral response was observed in the earlier experiments [19,20]. This phenomenon can be ascribed to the image force effect, which has been used to explain the voltage dependence of photocurrent observed in metal-SiO_2-Si structures [45] and Schottky barrier detectors [17]. This effect will be described as follows. A photoexcited carrier reaching the interface will be injected into the i-layer, provided that it can reach and surmount the interfacial energy barrier. The ability of a carrier to reach the barrier depends on the probability of scattering along the way, and in turn, depends on the distance of the energy barrier from the injecting interface. Both the barrier position and the barrier height are affected by the applied electric field due to the image force effect. As a result, the bias dependence of the photocurrent is determined both by the carrier scattering in the image force well and by the image force barrier lowering. The barrier lowering $\Delta\phi$ and the distance x_m from the interface to the barrier maximum are given by [46]

$$\Delta\phi = \left(\frac{qF}{4\pi\varepsilon_0\varepsilon_s}\right)^{1/2} \tag{14}$$

$$x_m = \left(\frac{q}{16\pi\varepsilon_0\varepsilon_s F}\right)^{1/2} \tag{15}$$

where $F = V_b/W_i$ is the electric field in the i-region, V_b the applied bias voltage.

The escaping carriers are subject to scattering out of the escape cone in passing from the injecting interface to the barrier maximum. The barrier collection efficiency η_c is defined as the probability that a carrier travels from the p^+(or n^+)-i interface to the barrier maximum without scattering. Since the emitted carriers travel essentially normally to the barrier, in first approximation, η_c is given by [17,45]

$$\eta_c = \exp(-x_m/L_s) \tag{16}$$

in which L_s is the carrier scattering length in the image force well (located in the i-layer). Here, we have neglected the energy dependence of L_s. The scattering mechanism is assumed to redirect the carrier momentum isotropically. It is assumed that no carrier is scattered more than once during its passage from the interface to the barrier maximum.

By taking the image force barrier lowering into account, the effective workfunction is $\Delta = \Delta_0 - \Delta\phi$, where Δ_0 is the zero field workfunction. This relationship can be used to explain the bias dependence of λ_c observed from experiments in Sec. 4.4.

 © 1999 COSiW SEP, Warsaw

3.5. Spectral response

The total quantum efficiency is the product of photon absorption probability, internal quantum efficiency and barrier collection efficiency,

$$\eta = \eta_a \times \eta_i \times \eta_c \qquad (17)$$

The responsivity is given by

$$R = q\eta\lambda g/hc \qquad (18)$$

where q is the elementary charge, g is the optical gain, h is the Planck constant, and c is the speed of light in vacuum.

By using the above analytic expressions, the responsivity for GaAs p^+-i structures has been calculated as functions of wavelength, electric field, and emitter layer doping concentration, etc. Unless indicated otherwise, the following parameters were used in the calculations: W_b = 100 Å, W_e = 150 Å, $N_b = 5\times10^{18}$ cm^{-3}, R_F = 0.3, R_B = 1, L_e = 4000 Å, L_p = 100 Å, L_s = 300 Å, and F = 1000 V/cm. For Ge and Si, in principle, similar analysis can be performed.

The effect of emitter layer doping concentration on spectral response is shown in Fig. 5 (i). Here four doping concentrations, $N_e = 5.0\times10^{18}$, 8.0×10^{18}, 1.0×10^{19}, and 1.5×10^{19} cm^{-3}, are used. It can be seen that with the increase of doping concentration, both the spectral bandwidth and the peak responsivity R_p increase, while the short wavelength side of the spectral response almost remains the same. It is noted that the spectra do not change continuously at low wavelength range, this is because in that photon energy range the internal quantum efficiency has different function relations with photon energy. The corresponding R_p, λ_c, and $\Delta\lambda$ (half-peak width) are: R_p = 0.20, 0.28, 0.32, and 0.47 A/W, λ_c = 180, 194, 209, and 287 μm, and $\Delta\lambda$ = 92, 96, 113, and 160 μm. The calculated R_p is in good agreement with the experimental results shown in sections 4 and 5 by taking into account the multilayer effects. As analysed before, the spectral response in the long wavelength side is governed by the internal photoemission mechanism, while in the short wavelength side it largely depends on the free carrier absorption mechanism.

The electric field dependence of spectral response is shown in Fig. 5 (ii). As F increases, both responsivity and λ_c increase considerably due to the image force effect, which is in good agreement with experimental results [19,20]. Also, the peak wavelength

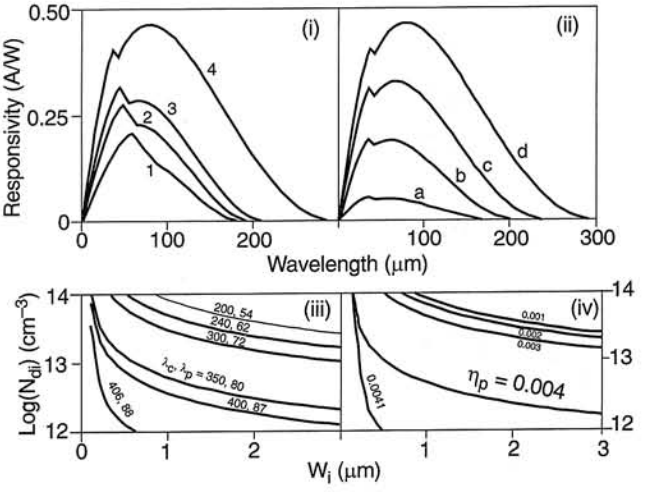

Fig. 5. (i) Spectral response calculated for four p-GaAs single layer detectors with the same electric field F of 1000 V/cm but different emitter layer doping concentrations N_e: (1) $N_e = 5.0\times10^{18}$ cm^{-3}; (2) $N_e = 8.0\times10^{18}$ cm^{-3}, (3) $N_e = 1.0\times10^{19}$ cm^{-3}, (4) $N_e = 1.5\times10^{19}$ cm^{-3}. (ii) The effect of electric field on spectral response is also shown for detector 4: (a). F = 50 V/cm; (b). F = 200 V/cm; (c). F = 500 V/cm; (d). F = 1000 V/cm. Contour plots of (iii) λ_c and λ_p in μm (the concentration of p^+ layers is 3.0×10^{19} cm^{-3} for the upper 4 curves and 3.2×10^{19} cm^{-3} for the bottom 2 curves), (iv) η_p (the concentration of p^+ layers is 3.0×10^{19} cm^{-3}) calculated for GaAs p^+-i-p^+ structure at an optimal electrical field F = 550 V/cm, as a function of N_{di} and W_i.

shifts gradually to longer wavelengths. In Fig. 5 (ii), for a device with $N_e = 1.5\times10^{19}$ cm^{-3} (Δ_0 = 7.58 meV) and W_e = 150 Å, as F increases from 50 to 1000 V/cm, Δ reduces from 7.3 to 4.3 meV, corresponding to an increase in λ_c from 170 to 287 μm, and R_p increases from 0.05 to 0.47 A/W. In order to get a higher responsivity, it seems that the applied bias should be as high as possible. However, in fact, there is an upper limit on applied bias or electric field (represented by V_c and F_c, respectively), due to the possible impact ionization breakdown of neutral impurity atoms occurring in the i-region. When $F > F_c$, the dark current will increase abruptly and the responsivity will decrease rapidly, which has been demonstrated by experimental results [20]. The quantum efficiency of the detector can be easily obtained by Eq. (18). The results show that even for the single layer structure a quantum efficiency up to about 1.0% for $N_e = 1.5\times10^{19}$ cm^{-3} may be reached. Figure 5 also shows the contour plots of the compensation concentration N_{di} vs i region thickness W_i for different emitter concentration detector samples

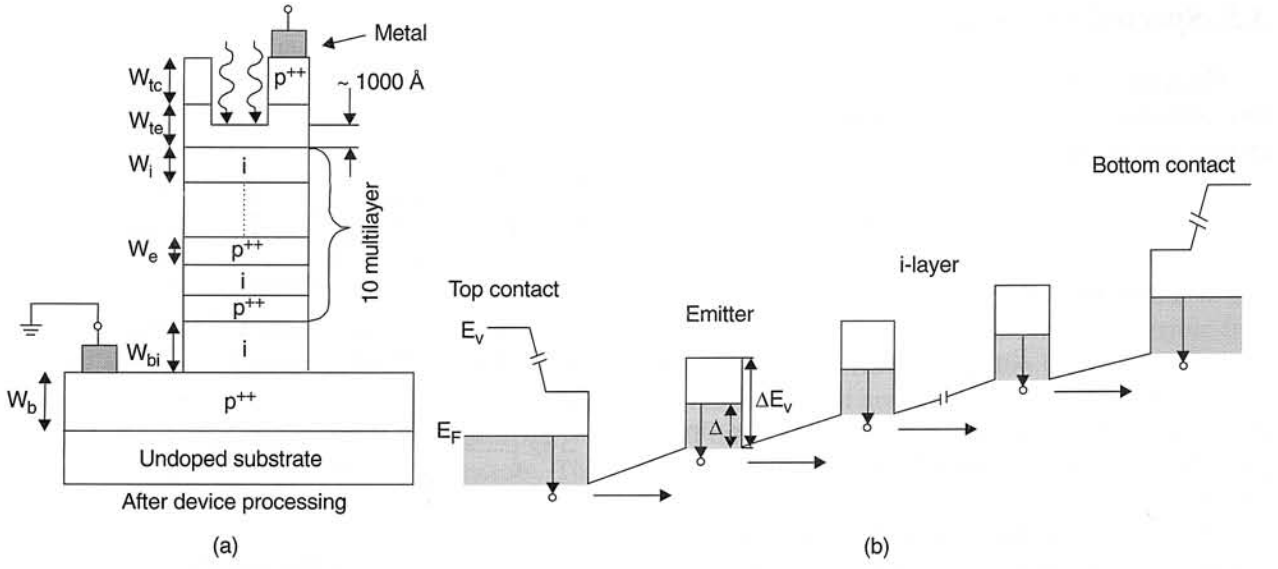

Fig. 6. (a) Schematic of 10 multilayer p-GaAs HIWIP detectors after device processing. p^{++}, p^+ and i are the contact layer, emitter layer and undoped layer, respectively. A window is opened on the top side for frontside illumination. (b) Energy-band diagram of the detectors under forward bias.

showing (iii) cutoff and peak wavelength λ_c, λ_p and (iv) peak quantum efficiency η_p. One important point to remember here is that the calculations are done for a single layer device. By using multilayer structures (p^+-i-p^+-i... or n^+-i-n^+-i...) and optimum emitter layer thickness, which can be realized by MBE or MOCVD growth technologies, the quantum efficiency can be easily improved, as shown experimentally in Sec. 5.1. It is also expected that the quantum efficiency may be further increased due to the increased photon absorption efficiency and possible photocurrent gain enhancement.

4. Effect of emitter layer concentration on the performance of GaAs p^+-i HIWIP FIR detectors

The recent rapid development of GaAs based long-wavelength quantum well focal plane array cameras [47] makes GaAs a promising candidate for developing HIWIP FIR detectors. We have successfully demonstrated the p-GaAs HIWIP FIR detectors using thin, highly doped p^+ and undoped i multilayer structures [48]. The thin emitter layer offers high internal quantum efficiency due to the low inelastic hole-hole and hole-phonon scattering, and the high doping concentration facilitates strong free carrier absorption. Multilayer structures are used to further increase the quantum efficiency due to the increased photon absorption efficiency and possible photocurrent gain enhancement [21], also demonstrated in stacked SiGe/Si heterojunction internal photoemission detectors [49].

A comparison of modelling and experimental results on the performance of p-GaAs HIWIP FIR detectors as a function of emitter layer concentration is first studied [50], since the emitter layer concentration plays a key role in the detector performance. In addition to the cutoff wavelength and responsivity, which are very important parameters for detectors, the dark current is another factor influencing the noise equivalent power (NEP) or detectivity D^* of detectors. The studies of dark current characteristics, cutoff wavelength, and the detector responsivity described here should lead to a clearer understanding of how the doping concentration affects the detector performance, which will be critical to detector design and optimization.

4.1. Experiment

Measurements were made on three p-GaAs FIR HIWIP detector samples (No. 9404, No. 9401, No. 9603) grown by molecular beam epitaxy (MBE) with the substrate temperature of 560°C. The MBE epilayers consist of a 4000 Å (W_b) bottom contact layer, a 1500 Å (W_{bi}) undoped layer, 10 periods of thin emitter (p^+) layers (thickness W_e of 150–300 Å) and udoped intrinsic (i) layer (thickness W_i of 1000 Å), and finally a 3000 Å (W_{te}) top emitter layer and a 3000 Å (W_{tc}) top contact layer. The emitter layers were doped with Be which has an ionization energy of 28 meV in p-GaAs. The doping concentration is between $(1–8)\times10^{18}$ cm^{-3}. The top and bottom contact layers were doped to $(2–3)\times10^{19}$ cm^{-3}, far above the Mott

 © 1999 COSiW SEP, Warsaw

Table 2. Parameters for six p-GaAs HIWIP FIR detector structures. Measured (from spectrum) interfacial workfunction Δ, peak quantum efficiency η_p, NEP, peak responsivity R_p, cutoff wavelength λ_c and calculated Fermi level from HD theory (E_F). The valence-band-edge offset is given by $\Delta E_v = \Delta + E_F$. Here, W_i, W_e, and W_{bi} are the thicknesses of the intrinsic (i), emitter (p^+), and bottom intrinsic (i), respectively. N_e and N_c are the doping concentrations of the emitter and contact layers, respectively. The thickness of the top contact (p^{++}), the top emitter (p^+) and bottom contact (p^{++}) layers, W_{tc}, W_{te}, and W_{bc} were 3000, 3000, and 4000 (3000 for No. 9604) Å, respectively, for six samples.

Sample No.	No. of layer	W_i (Å)	W_e (Å)	N_e (cm^{-3})	W_{bi} (Å)	N_c (cm^{-3})	Δ (meV)	E_F (meV)	ΔE_F (meV)	η_p %	NEP (10^{-12} W/Hz)	R_p (A/W)	λ_c (μm)
#9406	2	5000	300	1×10^{18}	1500	$2\text{–}3\times10^{19}$	~17.0	4.9	21.7	2.5	11.50	0.6	~75
#9405	5	2000	300	1×10^{18}	1500	$2\text{–}3\times10^{19}$	~17.0	4.9	21.7	5.7	3.76	1.4	~75
#9404	10	1000	300	1×10^{18}	1500	$3\text{–}4\times10^{19}$	16.8±0.2	4.9	21.7	4.8	2.77	1.2	76±1
#9401	10	1000	150	3×10^{18}	1500	$2\text{–}3\times10^{19}$	14.6±0.2	10.2	25.0	9.2	2.18	2.3	85±1
#9603	10	1000	150	8×10^{18}	1500	2×10^{19}	13.4±0.2	14.6	28.0	10.8	1.36	2.7	93±1
#9604	20	800	150	4×10^{18}	1500	2×10^{19}	12.4±0.1	12.3	24.7	12.5	0.44	3.1	100±1

transition value to ensure an ohmic contact. The schematic of the detectors after device processing and their energy-band diagram are shown in Fig. 6 with the key nominal sample parameters given in Table 2. Good control of MBE growth is indicated by secondary ion mass spectroscopy (SIMS) measurements (see Fig. 7). The contact was formed by deposition of Ti-Pt-Au.

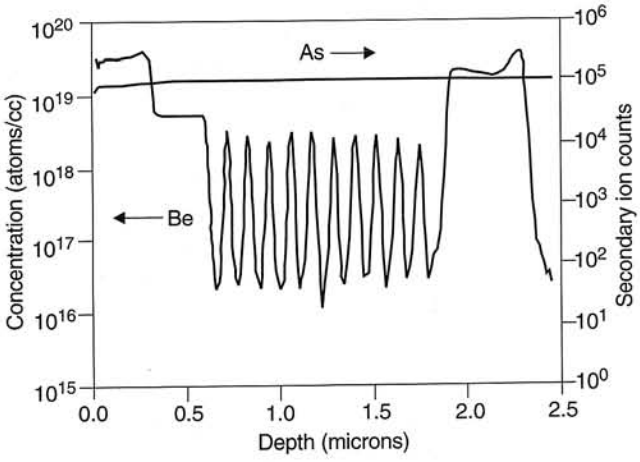

Fig. 7. SIMS profile of a Be doped p-GaAs HIWIP 10-layer detector sample No. 9401, indicating good control of multilayer interfaces in MBE growth. The background of As is near 10^5 atoms/cm^3.

4.2. Dark current characteristics

Unlike the case of GaAs/AlGaAs quantum well infrared photodetectors (QWIPs), where the current-voltage characteristics show asymmetric behavior under positive and negative biases normally due to the asymmetrical growth of GaAs/AlGaAs and AlGaAs/GaAs interfaces [47], the present GaAs homojunction FIR detectors display symmetric I–V characteristics. Figure 8 shows the dark I–V characteristics at 4.2 K for the three detectors under positive biases, together with

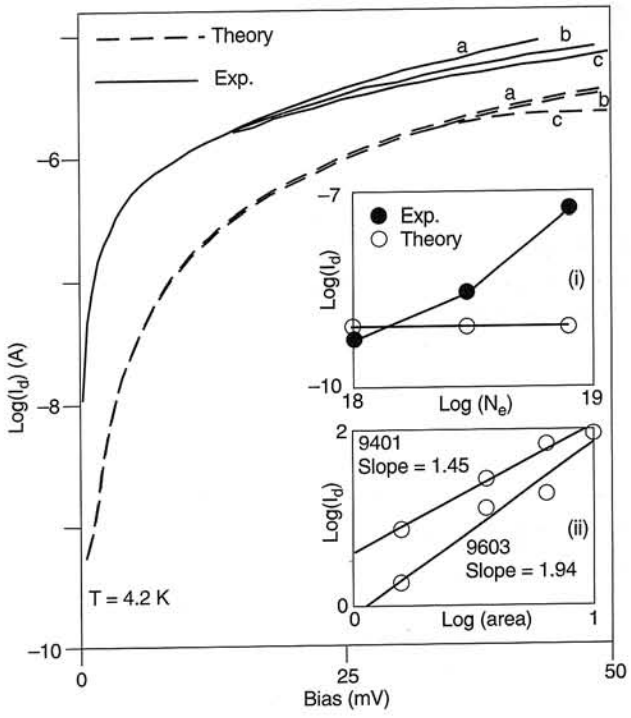

Fig. 8. Experimental (solid curves) and theoretical (dashed curves) dark current I_d characteristics at 4.2 K of p-GaAs HIWIP FIR detector sample: (a) No. 9404, (b) No. 9401, and (c) No. 9603. The inset (i) shows the experimental (solid circles, at 0.1 mV bias) and calculated (open circles, at 0.5 mV bias) I_d in the three HIWIP detectors at 4.2 K. The inset (ii) displays the log scale mesa area dependence of I_d of two samples at 10 mV forward bias (with a constant shift for clarity) and its regression slope, where we have neglected the orders of the current and area since there is only constant shift.

the dark current value near zero bias shown in the inset. It is seen that the three detectors display almost same dark current at high biases, in contrast to the case of near zero bias where the dark current increases rapidly with the doping concentration.

The dark current is modeled by assuming a uniform electric field in the multilayers, and thermodynamic carrier equilibrium. The properties of the multilayer detector are treated as repeat units, as in the case of QWIPs [47]. The energy band diagram for a HIWIP FIR detector should include both the multiple-image-force (MIF) and space-charge (SC) effects. The latter is due to the free-carrier spillover from the heavily doped layer into the undoped i layer. The dark current is the sum of space-charge-limited (SCL) current, thermionic emission (TE) current, and tunneling current, and as a good approximation, the SCL current, TE current and tunneling current can be treated separately [51].

At low temperatures required for the HIWIP detector operation, the effect of SCL current is clearly negligible. The TE current density is given by the Richardson-Dushmann equation

$$J_{TE} = A^{**}T^2 \exp\left(-\frac{\Delta}{k_B T}\right) \tag{19}$$

where A^{**} is the Richardson constant and k_B is the Boltzmann constant. The tunneling current is a combination of thermionic field emission (TFE) and field emission (FE), given by

$$J_t = J_{TFE} + J_{FE} = \frac{qm^*}{2\pi^2\hbar^3}\int |D(E)|T_t(E,E_\perp)dEdE_\perp \tag{20}$$

where $D(E) = f_e(E) - f_c(E)$, the difference of Fermi-Dirac distribution functions in emitter and collector layers, E the total energy of the tunneling holes, $E_\perp$ the transverse energy, and m^* the effective hole mass. T_t is the tunneling probability and can be obtained in the Wentzel-Kramers-Brillouin (WKB) approximation

$$T_t(E,E_\perp) = \exp(-2\int_{x_1}^{x_2} |k_x| dx) \tag{21}$$

where $|k_x|$ is the wave vector related with electrical field F in the tunneling direction, x_1 and x_2 are the classical turning points. The detailed expressions have been given elsewhere [25,51,52]. The total dark current is $I_d = A_0 (J_{TE} + J_{TFE} + J_{FE})$ with the detector area A_0 of 1.6×10^{-3} cm^2.

From the theory, it can be determined that the TFE is the major source of dark current in the p-GaAs HIWIP detectors at 4.2 K, so that small increase in dark current with increased doping is expected as a result of a slight modification to the Fermi-Dirac distribution. The dark current calculated for the three detectors is also shown in Fig. 8. The parameters for calculation can be found in Table 1, except the phonon scattering length and mobility, where 58 Å and 400 cm^2/Vs were used, respectively, for GaAs [46]. The dark current-voltage characteristics are almost independent of the doping concentration, in good agreement with the experimental results. Although the general trends are correct, it is noted that there is nearly an order of magnitude dark current difference between the experiment and theory. This fact is due to the existence of leakage current, which can be due to the surface or interface state defects [50]. Further evidence of this leakage can be seen from the experimental fact that the dark current increases superlinearly with the mesa area [see inset (ii) in Fig. 8], in contrast with the linear relation.

The calculated dark current near zero bias is also independent of the doping concentration [see inset (i) in Fig. 8], whereas the experimental data show a rapid increase with increasing concentration. This difference can be attributed to the existence of surface or interface defect states in the higher doping concentration samples. The origin of these defect states can be the dangling bonds in the interfaces, Coulomb potential of charged ions, and impurities near interfaces. The existence of surface or interface defect states can result in recombination via the defect states and generate tunneling current (it increases with the defect states and applied bias), which dominates the dark current at low biases. The high experimental dark current in the high doping emitter layer samples near zero bias can be attributed to the high tunneling current and is associated with high surface or interface defect states. However, with increasing bias, the contribution of thermionic field emission rapidly increases and dominates the dark current, resulting in almost the same experimental dark current at high biases even in different doping samples. Further evidence for the identification of these defect states can be clearly seen from the detector response spectra (e.g., Fig. 9), where remarkably reproduciable spike responses were observed in the spectra of highly doped emitter layer samples. One of the spikes was attributed to the localized nature of the defect states. Defects have been found to be the source of tunneling currents in HgCdTe detectors [53] and the elimination

 © 1999 COSiW SEP, Warsaw

of these imperfections is a significant material challenge yet to be overcome, and the defect induced current has also been found in advanced MBE technology for GaAs/AlGaAs QWIPs [47,54]. Recently, a successful approach reported in the literature described reduction of the dark current density due to the surface or interface defects by using thin films to passivate the detector surface [55], this may be beneficial to HIWIP detectors, especially the highly doped emitter layer samples.

4.3. Spectral response

The spectra of p-GaAs HIWIP detectors were taken with a Perkin-Elmer system 2000 FTIR spectrometer, with the samples mounted in a HD-3L dewar with a 15 μm cut-on cold filter. A Si bolometer was used as the reference detector to obtain the background spectrum and the responsivity. The bolometer, which has a flat response up to ~1 mm was calibrated using the load curve [56] and found to be (3.4±0.03) $\times 10^5$ V/W, in excellent agreement with the responsivity given by the manufacturer 3.4×10^5 V/W. Figure 9 shows the spectral responses measured at different forward biases for two samples of No. 9401 and No. 9404. A good qualitative agreement of theoretical model and experimental results can be seen by comparing Fig. 9 with Fig. 5. The long tailing behavior in the long wavelength region reflects the nature of internal photoemission.

Polarization-dependent response signal, as expected, showed to be independent of the polarization angle, which is indicative of a free carrier absorption in type II HIWIP detectors (see Fig. 10).

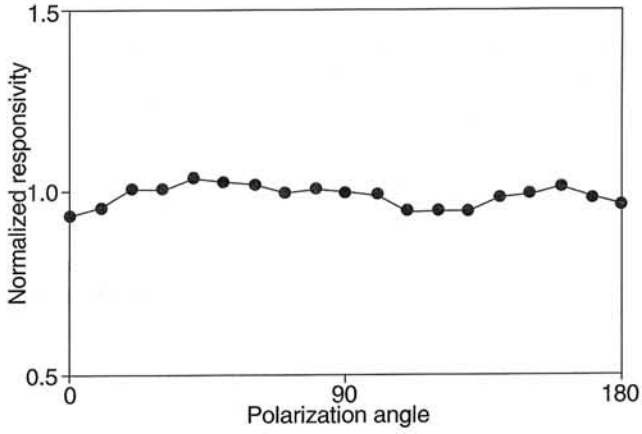

Fig. 10. Polarization dependence of the No. 9603 detector photosignal at a bias of 83.0 mV, which shows a free carrier absorption in HIWIP detectors.

The wavelength where the spectrum signal first reaches zero is at 92±1 μm for No. 9401 and 83±1 μm for No. 9404, corresponding to the Δ_s of $13.5^{+0.2}_{-0.1}$ meV and $14.9^{+0.2}_{-0.1}$ meV, respectively. The wavelength at which the mean (of at least 8 curves) response first reaches the same level as the maximum of the standard deviation of the spectra, (i.e., noise level), which was denoted as λ_c, is 85 ±1 μm for No. 9401 (at 193 mV bias) and 76 ±1 μm for No. 9404 (at 91.5 mV bias) as determined in Fig. 11. The effective barrier height of the HIWIP detector can also be determined by using an activation energy analysis of the thermionic current. The thermionic emission (dark) current I_d is given by

$$I_d \propto T^2 \exp\left(\frac{q\phi_B}{k_B T}\right) \tag{22}$$

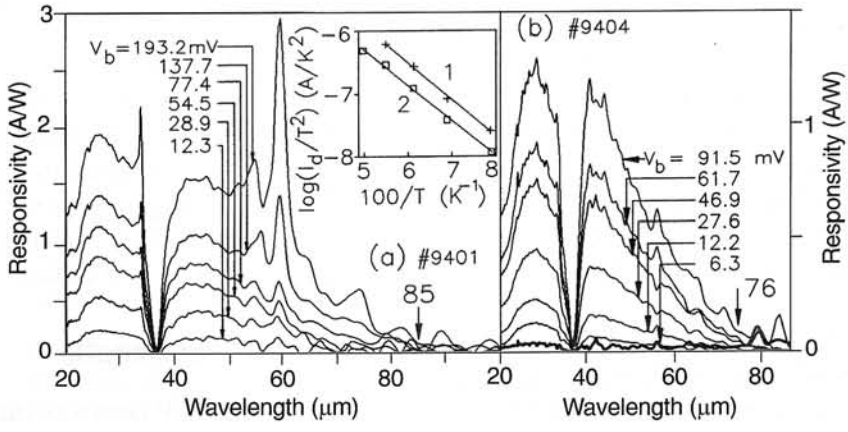

Fig. 9. Spectral response measured at 4.2 K for two samples at different forward biases: (a) No. 9401 with $N_e = 3\times10^{18}$ cm^{-3}, showing a cutoff of 85 ±1 μm. The deep valley at 36.5 μm is due to the transverse optical (TO) phonons of GaAs. The inset in (a) shows an Arrhenius plot for No. 9401 indicating a Δ of 11.6 ±0.4 meV at 12 mV (labeled as 2) and 11.2 ±0.4 meV at 6 mV (labeled as 1) corresponding to an even longer λ_c. (b) No. 9404 with $N_e = 1\times10^{18}$ cm^{-3}, showing a cutoff of 76 ±1 μm.

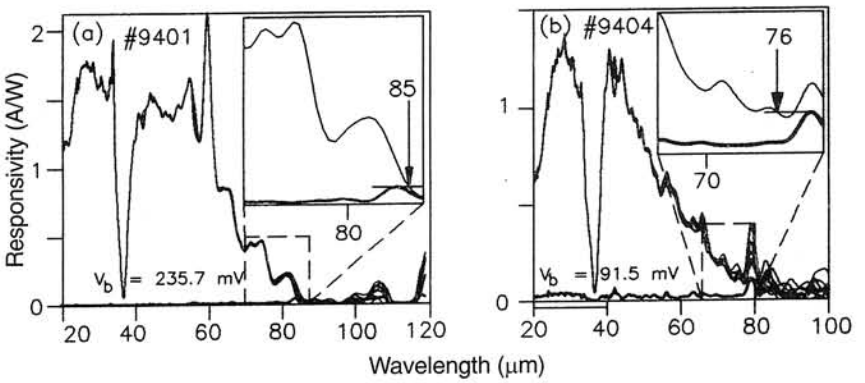

Fig. 11. (a) Spectral response for No. 9401 taken at 235.7 mV repeated for 8 times over a period of 5 hours. The peak at around 60 μm exhibit excellent overlap in the 8 curves as seen, confirming that it could not be due to noise. The dark line indicates the deviation (noise level) curve. (b) The spectral response for No. 9404 taken at 91.5 mV repeated for 16 times over a period of 10 hours, with the standard deviation (dark curve). The insets in (a) and (b) are the blow ups of the marked area of the mean and the deviation curves to show the determination of λ_c.

where T is the absolute temperature, and $q\phi_B$ is the thermal potential barrier height above the Fermi level. The detector dark I-V characteristics were measured down to 1.6 K and found that the dark current has a strong temperature dependence above 12 K. The inset in Fig. 9(a) show an Arrhenius plot (of dark current vs reciprocal temperature,) for No. 9401 resulting in a $q\phi_B$ of 11.2 ±0.4 meV at 6 mV bias (labeled 1) and 11.6 ±0.4 meV at 12 mV bias (labeled 2) indicating λ_c is even longer than 92 μm.

The optical barrier height Δ determined by spectral response measurements is usually larger than the thermal potential barrier $q\phi_B$ [9]. The discrepancy results mainly from the energy loss of the photoexcited carriers by inelastic scattering prior to the carrier emission. On the other hand, this difference can help to identify the free carrier absorption mechanism in detectors. The very small energy difference (~3 meV) in the HIWIP detector shows that the photoexcited holes suffer less inelastic scattering in the emitter layers and the free carrier absorption mechanism in HIWIP is an acoustic phonon-emission assisted process. In contrast, the absorption in GeSi/Si structures at 80 K is an optical phonon-emission assisted process [57]. This is due to the low temperature operation of HIWIP structures. This result also indicates that the GaAs HIWIP FIR detector is an efficient detector, suitable for FIR detection.

The responsivity curves show a strong bias dependence, increasing significantly with increasing bias. However, the bias cannot be increased indefinitely as the dark current also increases with bias. The λ_c also shows a strong bias dependence in the low bias range as seen before. The spectral response at reverse biases is similar to that at forward biases, but the responsivity is somewhat smaller as expected since the top emitter has no contribution to photocurrent for the reverse bias case. It is noted that the spectral response exhibits a deep valley between 35 and 40 μm. The valley minima correspond to the transverse optical phonon energy in GaAs [58]. The peak near 35 μm associated with the absorption minima at 36 μm is a characteristic feature of GaAs absorption and reflection curves [58]. The sample No. 9401 exhibits remarkably reproducible spike responses at 34.0 and 59.5 μm, which are not due to noise as is evident from Fig. 11. This becomes stronger with increasing bias as shown in Fig. 9(a). Their origins can be due to the local vibrational mode (LVM), hydrogenic transitions and the defects in the samples. Experimental results show that it almost disappears in lower doped emitter layer samples [see Fig. 9(b)] and its position also changes with different doping concentrations. The hydrogenic transitions of Be acceptor impurity 1s to 2p, 3p, 4p, and continuum are expected at 59.1 μm, 49.8 μm, 47.2 μm, and 44.3 μm, respectively. Here the peak at 59.5 μm which is between 44 and 60 μm could be the 1s → 2p transition. The LVM absorption of Be impurities in GaAs was reported at 20.7 μm in literature corresponding to the 100% abundant $^9Be_{Ga}$ acceptors [59]. This indicates that the 34.0 μm structure is mainly associated with the defects in the surface or interfaces of the sample.

4.4. Cutoff wavelength

The λ_c of HIWIP detectors shows strong bias and emitter layer concentration dependences due to the MIF effects and band edge lowering. The longest λ_cs obtained from the responsivity spectra are 76 ±1 μm for No. 9404 at 91.5 mV bias, 85 ±1 μm for No. 9401

 © 1999 COSiW SEP, Warsaw

at 193.0 mV bias, and 93 ±1 μm for No. 9603 at 157.0 mV bias. The lowering of the band edge due to high doping can be described using the high density (HD) theory in Sec. 2. However, the Fermi level E_F determined by using the conventional density of state [Eq. (3)] is considerably larger than the value determined directly from the observed luminescence spectra [34]. A comparison of the calculated results from Eq. (3) with the luminescence results [34] gave, for p-GaAs, a difference of about 5 ±1 meV for doping concentrations between 1×10^{18} to 5×10^{19} cm^{-3}, and even smaller differences with higher concentrations. This difference is included here by using a modified Fermi level expression: $E'_F = E_F - 5 \pm 1$ meV, so the workfunction used is

$$\Delta = \Delta E_{maj} - E'_F - \sqrt{\frac{qF}{4\pi\varepsilon_0\varepsilon_s}} \qquad (23)$$

where the last term is the image force barrier lowering due to the electric field F.

Using Eq. (23) and equations in Sec. 2.4, the doping concentration dependence of ΔE_{maj} and Δ at zero bias was calculated, as shown in Fig. 12, together with the experimental workfunction results [corrected to very low bias by Eq. (23)] by solid circles. It is seen that the experimental λ_c is in reasonable agreement with the calculations using the HD theory. This result demonstrates: (i) the successful fabrication of GaAs HIWIP FIR detectors using the interfacial work function, (ii) the reliability and simplicity of HD theory in calculating the shift of the band edge in highly doped semiconductors. On the other hand, much longer λ_c GaAs HIWIP detectors could be obtained by employing the emitter layer concentration in the order of 10^{19} cm^{-3}, since, from the HD theory shown in Fig. 12, only a small increase in doping concentration can cause a large decrease in work function Δ (large increase in λ_c).

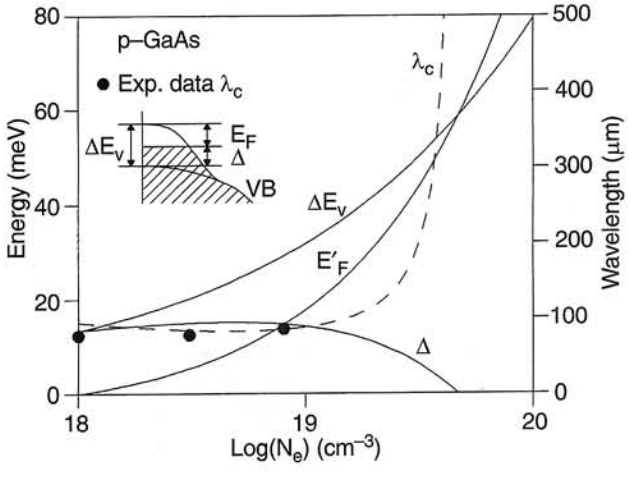

Fig. 12. Calculated emitter layer doping concentration N_e dependence of the shift for the major band edge ΔE_{maj} and interfacial work function Δ at zero bias from the high density (HD) theory. The theoretical curve of Δ should have a deviation of ±1 meV due to the modified Fermi level (see text). The experimental work function results [corrected to very low bias by Eq. (23)] are shown by solid circles.

4.5. Responsivity

A high free carrier absorption coefficient (10^3–10^4 cm^{-1}) in FIR range is an important advantage for HIWIP detectors. Also the absorption coefficient is almost independent of temperature due to the almost temperature invariant carrier concentration and mobility. The responsivity of a HIWIP detector is proportional to its total quantum efficiency, which is the product of photon absorption probability, internal quantum efficiency, and barrier collection efficiency. Since the Fermi level E_F, work function Δ and hole mobility do not change very much with the hole concentration in the experimental region (1×10^{18} – 8×10^{18} cm^{-3}), it is assumed that the internal quantum efficiency and barrier collection efficiency do not change with the doping concentration. All three detector samples have 10 multilayers, hence they should have the same photocurrent gain enhancement. Taking these into account, the variation of the detector responsivity with the doping concentration should follow that of the absorption probability.

The photon absorption probability for N multilayer HIWIP detectors can be calculated as

$$\eta_a = (1 - R_F)[1 - \exp(-N\alpha_e W_e)] \qquad (24)$$

where α_e is the free carrier absorption coefficient in emitter layer (thickness W_e). By using the experimental relationship in Eq. (11) and $R_F \approx 0.3$, and the layer parameters of the detectors, the photon absorption probability was calculated for HIWIP detectors as a function of carrier concentration, and compared with the experimental results for detector responsivity near 50 mV forward bias, shown in Fig. 13. Due to the difference in the parameter of W_e (see Table 2) from the other two detectors, the experimental responsivity of detector No. 9404 has been scaled to the same parameters as No. 9401 and No. 9603 by comparing with the different absorption probability in No. 9404. The experimental responsivity of the detectors follows the absorption probability well. The small deviation at high concentration is due to the

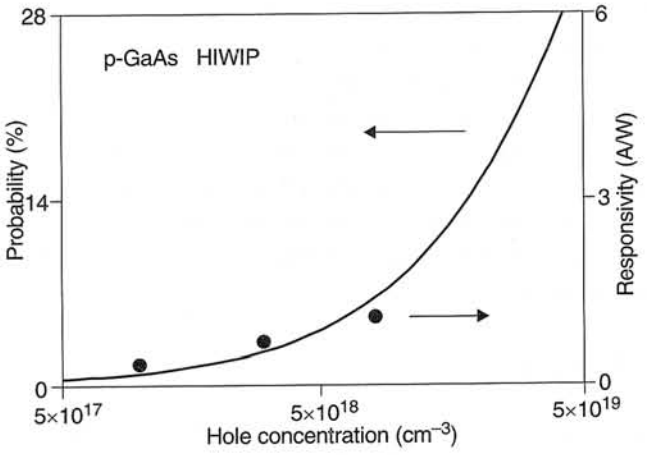

Fig. 13. Theoretical (solid curve) photon absorption probability as a function of hole concentration by using the linear relationship [Eq. (11)] shown in the inset of Fig. 4 and the 10 layer detector structure parameters given in Table 2. Solid circles are the experimental detector responsivity near 50 mV forward bias.

slight decrease in diffusion length, which affects the collection efficiency. Furthermore, it can be seen that the photon absorption probability increases rapidly when the hole concentration increases from 1×10^{19} to 4×10^{19} cm^{-3}. Since the collection efficiency changes much less than the absorption probability, this strong enhancement of the photon absorption probability with the carrier concentration shows that highly doped (~10^{19} cm^{-3} order) emitter layers are more attractive for higher quantum efficiency (and responsivity) in p-GaAs HIWIP FIR detectors.

5. High performance p-GaAs HIWIP FIR detectors

This section reviews a high performance p-GaAs HIWIP FIR detector [60] with the emphasis on responsivity (quantum efficiency), cutoff wavelength, detectivity, uniformity, crosstalk, photoconductive gain, response time, and noise characteristics.

The p-GaAs FIR HIWIP detector sample (No. 9604) was grown and fabricated as before. The MBE epilayers consist of a 3000 Å bottom contact p^{++} layer, a 1500 Å undoped (i) layer, 20 periods of thin emitter p^{+} layers (thickness 150 Å) and undoped i layers (thickness 800 Å), and finally a 3000 Å top emitter layer and a 3000 Å top contact layer. The emitter layers were doped with Be to 4×10^{18} cm^{-3}. The top and bottom contact layers were doped to $(2–3)\times10^{19}$ cm^{-3}, far above the Mott transition value to ensure an ohmic contact. Secondary ion mass spectroscopy (SIMS) measurements confirmed the doping levels and profile.

5.1. Responsivity and quantum efficiency

The responsivity R spectra of the p-GaAs HIWIP FIR detector under different forward biases at 4.2 K are shown in Fig. 14. These responsivity curves show the same behavior as before. The responsivities are larger than the previous results as this structure has 20 multilayers. The highest responsivity obtained here is 3.10 ±0.05 A/W at a bias of 192.0 mV. Figure 15 shows the bias dependences of the detectivity D^* and peak quantum efficiency η_p determined from Eq. (18) with g = 1. The quantum efficiency η (responsivity) is roughly linear under low biases and gradually saturates at high biases. However, the detectivity is almost independent of the applied bias and the maximum detectivity occurs at a bias just below the value at which the quantum efficiency (responsivity) saturates, as in the case of GaAs/AlGaAs quantum well infrared photodetectors [47]. At high biases, the dark current increases rapidly thereby reducing D^*. At low biases, the barrier collection efficiency η_c decreases, lowering D^* (discussed further below). Thus, D^* appears relatively insensitive to bias. The highest detectivity is 5.9×10^{10} cm$\sqrt{\text{Hz}}$/W at 4.2 K under a bias of 83.0 mV. This value is at least five times larger than the value reported [48] (see Table 2) due to both high responsivity (multilayer effect) and low dark current (good sample quality and device processing).

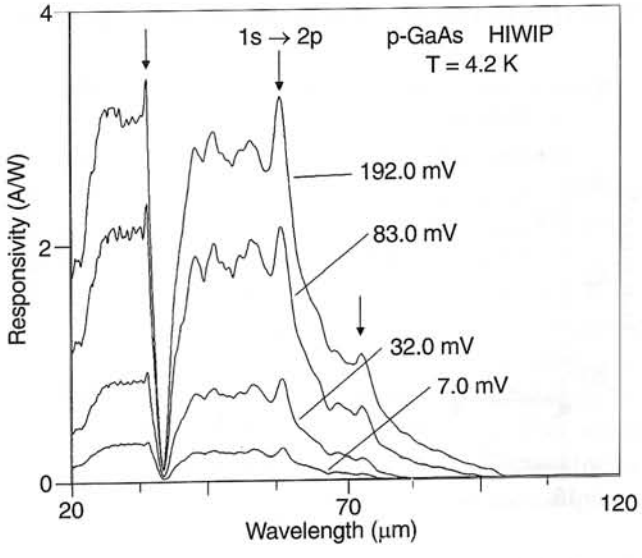

Fig. 14. Spectral response of p-GaAs HIWIP FIR detector measured at 4.2 K under different forward bias values. The deep valley at 36.5 μm is due to the transverse optical (TO) phonons of GaAs. The structures marked with arrows are believed to be related with interface states. The hydrogenic excited states of the Be acceptors are expected to show structures between 44 and 60 μm.

 © 1999 COSiW SEP, Warsaw

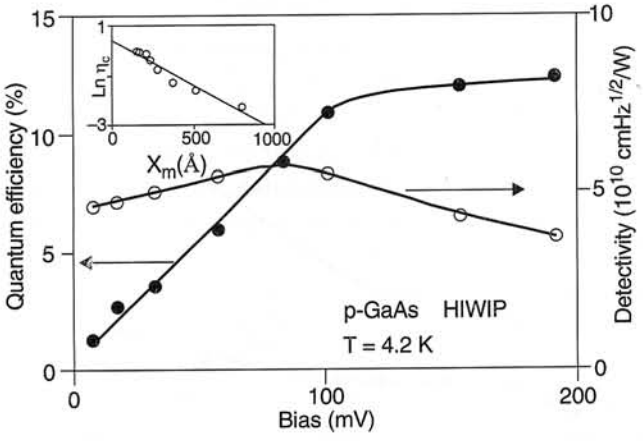

Fig. 15. Bias dependences of peak quantum efficiency measured at 30.0 μm (filled circles) and device detectivity (open circles). Shown in the inset is the semi-log plot of the barrier collection efficiency as a function of x_m, the distance from the interface to the barrier maximum, which is bias dependent.

The maximum quantum efficiency in HIWIP FIR detectors can be estimated by taking into account the free carrier absorption and inelastic scattering loss. By assuming a constant inelastic scattering mean free path L_z and a constant absorption coefficient α_p in an emitter layer of thickness W_e with 2(N + 1) optical passes due to multilayer N structures (1 comes from an additional stacked layer), the maximum quantum efficiency is given by

$$\eta_{\max} = \{1-\exp[-2(N+1)\alpha_p W_e]\}\exp\left(-\frac{W_e}{L_z}\right) \approx \approx 2(N+1)\alpha_p d \times \exp\left(-\frac{W_e}{L_z}\right) \quad (25)$$

Using the concentration P, dependence of the absorption coefficient of Eq. (11) with P = 4×10^{18} cm^{-3}, 20 multilayers (N = 20), a typical value of $L_z \approx 200 \sim 300$ Å in p-GaAs [61], and an emitter layer thickness of 150 Å, we get η_{max} = 12.7% in the present GaAs detector, in good agreement with the experimental result of 12.5% at a bias of 192.0 mV shown in Fig. 15. Two other detector samples with 10 multilayers (N = 10) and a single layer (N = 0) were also measured, with all the other parameters the same, and the maximum quantum efficiency was 6.1% and 0.5%, respectively, consistent with the theoretical prediction of 6.6% and 0.6%. In addition, an optical cavity would gain another factor of two in the optical pass.

5.2. Bias dependence characteristics

The bias behaviour of the quantum efficiency in Fig. 15 results from the fact that the net quantum efficiency has two components. One is η_{max} as discussed in Sec. 5.1 (including both the photon absorption probability and internal quantum efficiency), and the other is the barrier collection efficiency η_c, which is bias dependent due to the image force effect. A semi-log plot of η_c as a function of x_m is shown in the inset of Fig. 14. The linear relation demonstrates that the experimental results can be well described by above simple approximation. The solid line in the figure corresponds to the regression of the experimental data, which yields the hole scattering length L_s of 276 ±2 Å in p-GaAs. In terms of the above model, the effect of bias-independent scattering mechanisms such as those due to interface states has been lumped as a constant.

The responsivity curves shown in Fig. 14 also display a strong bias dependence of cutoff wavelength λ_c, increasing with the applied bias due to the image force effect. The experimental data are shown as solid circles in Fig. 16. The theoretical λ_c (solid curve) is calculated by Eq. (23). It is seen that the experimental λ_c is in good agreement with the calculation with a maximum deviation of 1.0 meV. The λ_c is tunable with applied bias voltage (from 80 ~ 100 μm for a bias range of 7 mV to 192 mV), and can also be tailored through the emitter layer doping concentration. However, the experimental λ_c decreases with the increase of applied bias under very high biases. The cause of this experimental result, though not well understood, is thought to be due to hot carrier effect [62]. Under high electrical fields or strong irradiation, the temperature of carriers in semiconductors increases and the states above Fermi level are occupied by localsed carriers [62]. Here, a bias of 192.0 mV (cor-

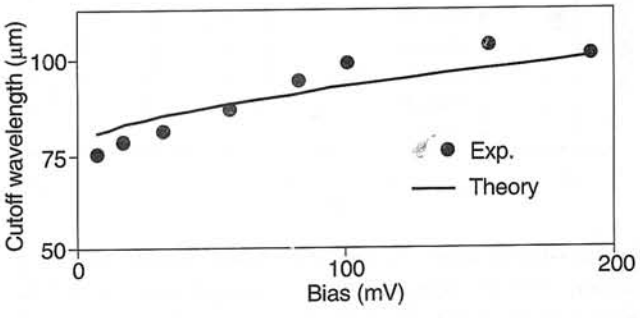

Fig. 16. Bias dependence of cutoff wavelength in the p-GaAs HIWIP detector at 4.2 K. The maximum deviation between the theory (solid curve) and experiment (filled circles) is 1.0 meV.

responding to an electrical field ~1.2×10^3 V/cm) resulted in a dramatic decrease of the photoconductivity signal near λ_c.

5.3. Uniformity and crosstalk

In addition to studying the effect of the number of layers, the bias dependence of the quantum efficiency, D^*, and λ_c, the uniformity of the detectors was also tested. The dark current of 7 randomly chosen relatively large mesas (460 μm × 460 μm) at 4.2 K was quite uniform (as shown in the inset of Fig. 17) with a standard deviation of 15.4% at a bias voltage of 200 mV. Furthermore, the bias dependence of D^* for the 7 mesas is shown in Fig. 17, the values are within experimental errors. The relatively low D* can be due to dark current leakage in larger mesas. These results clearly demonstrate the possibility of high uniformity required for large FIR focal plane arrays, since the typical pixel size for arrays is much smaller than the tested devices, (e.g., 50 μm × 50 μm in GaAs/AlGaAs QWIPs [47], and thus the dark current per pixel, together with the standard deviation, would be about two orders of magnitude smaller.

Figure 18 shows the crosstalk of the p-GaAs HIWIP FIR detector measured by focusing the incident light spot on one mesa and monitoring the photoconductivity outputs of the adjacent mesas. Output photoconductivity signal when the light is on mesas (a) and as a percentage of direct incident signal (b).

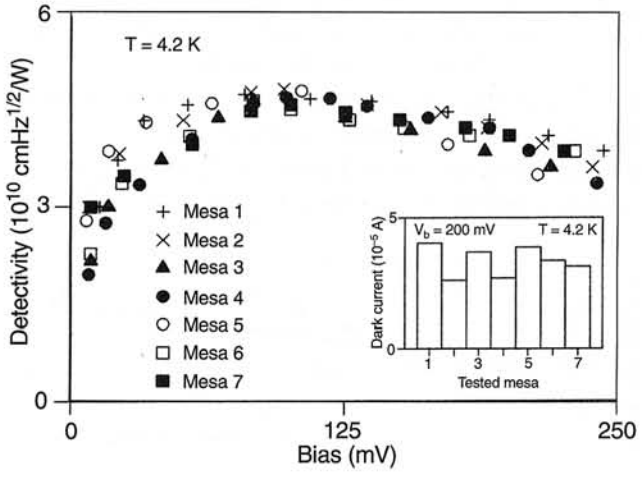

Fig. 17. Bias dependence of device detectivity of 7 randomly chosen 460 μm-square mesas at temperature of 4.2 K. Shown in the inset is the dark current of the 7 mesas at 4.2 K and a forward bias of 200 mV. Some dark current leakage is observed in these larger mesas. The uniformity of the p-GaAs HIWIP FIR detector is demonstrated by both the uniform dark current and detectivity.

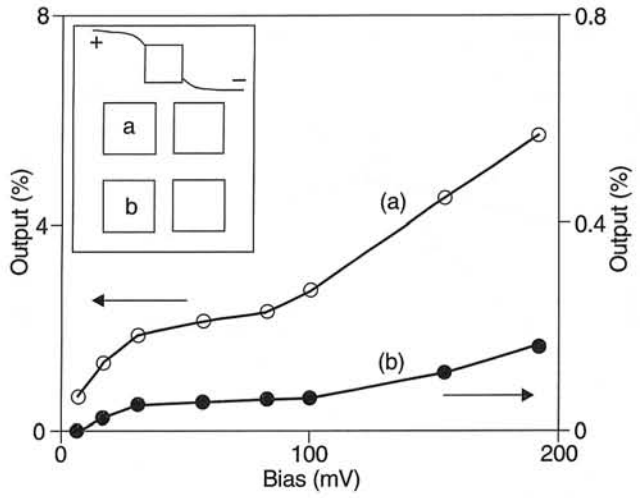

Fig. 18. The crosstalk of p-GaAs HIWIP measured by focusing the incident light spot on one mesa and monitoring the photoconductivity outputs of the adjacent mesas. Output photoconductivity signal when the light is on mesas (a) and as a percentage of direct incident signal (b).

At the bias with the highest detectivity (83.0 mV), the crosstalk is found to be 2.29% for mesa (a) and 0.061% for mesa (b). The maximum output percentage (5.70% and 0.16%) corresponds approximately to the maximum output of the device (at 192.0 mV). Lower values of crosstalk have been achieved under various bias conditions. This crosstalk is comparable to 2.1% (in the first nearest column case) in Si:As BIB detectors [63].

5.4. Photoconductive gain

The study of photoconductivity generation mechanism and photoconductive gain can help us obtain a clear physical understanding of the device operation. In QWIPs, the photoconductive gain has been widely studied [47,64–66], which has shown that the photoconductive gain is inversely proportional to the number of quantum wells and that the current responsivity is independent of the number of wells. However, in internal photoemission infrared detectors, the current responsivity R and quantum efficiency η increase with the number of emitter layers due to the multilayer effect [67,68]. The responsivity is related to gain g by Eq. (18). There is no detailed study of photoconductive gain in internal photoemission detectors in the literature [68].

Unlike the usual interband transition, where both electrons and holes can be created when the optical energy hv is greater than the energy gap E_g, and the semiconductor does not need to be doped, the

 © 1999 COSiW SEP, Warsaw

intersubband based QWIPs must be doped since $h\nu < E_g$ and thus the photon energy is not sufficient to create photocarriers. The photocarrier generation mechanism is an excitation of an electron (hole) from the doped quantum well ground state in the conduction (valence) band to an unoccupied excited or continuum state in the same band. These QWIPs are somewhat analogous to extrinsically doped semiconductors, but with much larger optical transition dipole moments [69]. Therefore, only one kind of photocarriers (electrons in n-type, and holes in p-type) can be created in QWIPs, and an extra current from a contact is necessary to balance the loss of photocarriers from the well due to photoemission. The photoconductivity comes from the variation of the carrier concentration and the total photoconductivity consists of contributions from direct photoemission and the extra current injection, which can well explain the experimental observations of large (>> 1) photoconductive gain and its inverse proportionality to the number of wells [64,65].

In internal photoemission junction detectors, the incident photons are absorbed in the emitter layers by the free carrier absorption mechanism, and under suitable bias conditions the photoexcited carriers with energy $h\nu$ larger than the band-edge offset between the doped emitter layer and the undoped transit region Φ ($h\nu > \Phi$) are emitted across the junction and then collected. For a homojunction, the band offset is determined by the doping-induced bandgap narrowing of the emitter region, while for the heterojunction (e.g., GeSi/Si) it depends on the alloy bandgap [11]. In both cases, electrons and holes will be created and the carrier concentration in emitter layers remains constant. The increase of hot carrier energy will alter its mobility from its equilibrium value, since the mobility is determined by the ionized impurities and energy-related scattering processes. Therefore, it is the change in mobility of the hot carriers that results in the photoconductivity, which mainly depends on the free carrier absorption and photocarrier relaxation processes [70]. This hot carrier effect can well explain the experimental (gain and responsivity) results, without an extra current injection [71,72].

After photogenerated carriers created in the emitter layers by free carrier absorption due to optical illumination, they are either swept out by electric field to generate photocurrent, or else they are captured by the emitter layer and recombine. The ratio of the number of photocarriers collected to the number of photons absorbed (exclude inelastic scattering loss) is conveniently expressed as the barrier collection efficiency η_c. This is equal to the ratio of the sweep-out rate and the total carrier loss rate (sweep-out and recombination)

$$\eta_e = \frac{1}{\tau_s} \Big/ \left(\frac{1}{\tau_s} + \frac{1}{\tau_r} \right) \equiv 1 - P_c \tag{26}$$

where τ_s is the sweep-out time, τ_r is the recombination time, and $P_c \equiv \tau_s/(\tau_r + \tau_s)$ is the capture or trapping probability as defined in QWIPs [47,65].

The infrared photo-ionized holes in the emitter layers drift through the undoped i-regions and contribute to the photocurrent. Taking into account the fact that the photon flux could depend on the location of the emitter layers, the photocurrent directly ejected from the n^{th} emitter layer is

$$i_p^{(n)} = eI_F \eta^{(n)} \eta_c (1 - P_c)^{n+} \tag{27}$$

where I_F is the photon flux in the first emitter layer, and $\eta^{(n)}$ is the quantum efficiency for a single n^{th} emitter layer. The total quantum efficiency η in N multilayer internal photoemission detectors can be calculated by taking into account the free carrier absorption and inelastic scattering loss. From Eq. (25), we have: $\eta \approx N\eta^{(n)}$, since α and d are usually in the orders of 10^3 cm^{-1} and 10^{-6} cm, respectively.

Since there is no contribution from the extra injection in internal photoemission detectors, the photocurrent collected in the collector contact from all the emitter layers is

$$I_p = \sum_{n=1}^{N} i_p^{(n)} = eI_F \frac{1}{N} \eta \eta_c \frac{1 - (1 - P_c)^N}{P_c} \tag{28}$$

The experimental quantum efficiency of HIWIP detectors shows a good agreement with the theory in Eq. (25) confirming that the barrier collection efficiency η_c is nearly 100% at higher bias values. Thus further increase in bias is not expected to lead to a significant increase in responsivity, as shown by the saturation behavior of the responsivity. Furthermore, the recombination time should be much longer since the internal photoemission far infrared detectors operate at low temperatures and very long wavelengths, where acoustic phonon scattering plays an important role. These results show that P_c could be much less than 1. As a result, Eq. (28) becomes

$$I_p = eI_F \eta \eta_c \tag{29}$$

Therefore, the photoconductive gain of an internal photoemission infrared detector is independent of the number of emitter layers

$$g = 1 - P_c \tag{30}$$

which is less than but close to 1 due to weak capture probability. In addition, for the worst case of assumption $P_c << 1$ in a single emitter layer structure, the above equation can be directly obtained form Eq. (28). However, the responsivity $[I_p/(hvI_F)]$ is proportional to the number of emitter layers since $\eta \propto N$ as seen in Eq. (25). The conclusion is in contrast to that of QWIPs due to the different photocarrier generation mechanisms.

The photoconductive gain g and responsivity R versus number N of emitter layers for the p-GaAs homojunction internal photoemission far-infrared detector are shown in Fig. 19. The gain values are calculated from the combination of response and absorption measurements as discussed in Ref. 47. As shown in Fig. 19, the photoconductive gain values are independent of N and are actually less than but close to 1, while the responsivity is proportional to the number of emitter layers. In addition, the photoconductive gain in a p-GeSi/Si heterojunction internal photoemission detector (3 multilayer) is also estimated to be 0.93, based on the experimental results of quantum efficiency and absorption, which are in good agreement with the theoretical conclusions obtained above

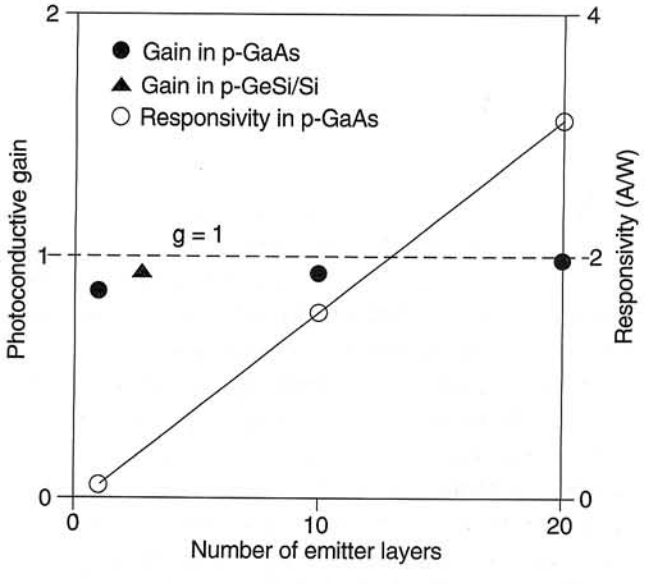

Fig. 19. Experimental photoconductive gain and current responsivity versus number of emitter layers in p-GaAs homojunction and p-GeSi/Si heterojunction internal photoemission infrared detectors.

[68]. The relatively small increase in gain with increasing number of layers, for example, the gain values for 1, 10, 20 emitter layers are 0.834, 0.925, 0.983, as seen in Fig. 19, is due to the weaker capture probability for more layers, possibly as a result of impact ionization of photocarriers [21].

5.5. Response time

FIR (≥ 50 μm) detectors have typically been expensive and/or difficult to fabricate. Most commercial detectors in that wavelength are thermal detectors such as bolometers and pyroelectric detectors which tend to have slow response times. The photodetection mechanism of the HIWIP FIR detectors suggests that this type of detectors may meet the recent attempts to extend fast photoconductors into FIR range. In QWIPs operating in mid-infrared wavelengths (4–20 μm), the response times have been widely studied [47,65,73,74], showing the intrinsic high speed.

The response time of the p-GaAs HIWIP detector can be estimated from the bias dependent responsivity measurements [75]. Under light irradiation, excited carriers are generated by free carrier absorption in the valence band, however, the total number of carriers remains constant with an effective temperature T_e (deviation from equalibrium temperature T_0) in a hot carrier population. The photoconductivity is given by

$$\Delta\sigma = qP[\mu(T_e) - \mu(T_0)] \tag{31}$$

where P is the carrier concentration, μ is the mobility. For a slight heating of the carriers, we have

$$\Delta\sigma = qP\frac{\partial\mu}{\partial T}\bigg|_{T=T_0}(T_e - T_0) \tag{32}$$

Therefore, the photoconductivity is directly related to the transport properties of the hot carriers. The temperature rise $T_e - T_0$ has now to be related to the incident power

$$\frac{Pk_B(T_e - T_0)}{\tau} = \frac{I_0\eta}{A_0 D} \tag{33}$$

where τ is the energy relaxation time of the hot carriers, which in the limit can be regarded as the detector response time. The left term of Eq. (33) represents the power transferred to the lattice by the hot carriers, while the right term displays the power transferred to the hot carrier distribution.

 © 1999 COSiW SEP, Warsaw

The current responsivity R under the bias voltage V can be expressed

$$R = \frac{q\eta\tau}{k_B D^2}\left(\frac{\partial\mu}{\partial T}\right)\Bigg|_{T=T_0} V \qquad (34)$$

Using the temperature dependent mobility [76] ($\mu \propto T^{3/2}$) due to the ionized impurity scattering for the low experimental temperature of $T_0 = 4.2$ K, the current responsivity can be rewritten as

$$R = \frac{3q\eta\mu\tau}{2D^2}\frac{1}{k_B T_0} V \qquad (35)$$

Figure 15 has shown the bias dependence of quantum efficiency (responsivity) measured at 4.2 K. The measured quantum efficiency (responsivity) increases linearly with the bias at low bias voltages as Eq. (35) predicts. The saturation of the quantum efficiency (responsivity) at high biases is due to the quasi-depletion of the impurity band as proposed in a simple recombination model [38]. For a given bias, the responsivity is proportional to the response time, which is the same as in the case of intrinsic or extrinsic photoconductive detectors. Taking the total absorption quantum efficiency of 12.7%, detector thickness D of 1.6 μm, measured mobility of 60 cm^2/Vs for similar doping levels [37], and the slope of 24.2 A/WV in linear region of R vs V graph in Fig. 15, the response time of the detector is estimated to be about 20 ps, corresponding to a cutoff frequency of 8.0 GHz. This result is close to the high speed GaAs/AlGaAs QWIPs [47,73,74] and shows the suitability of HIWIP detectors for high-speed heterodyne applications.

5.6. Noise measurements

Noise measurements provide a valuable diagnostic tool for the evaluation of electric and optoelectronic devices and their long-term performance. Characterization of low frequency noise in HIWIP FIR detectors [77] is useful not only for improving the device performance, but also for getting information about the physical properties, such as interface states, gain, etc.

The noise characteristics were measured using a low noise preamplifier (SR 560) and a fast Fourier transform (FFT) spectrum analyzer (SR 780) with the detector temperature at 4.2 K. The equipment was calibrated by measuring the room temperature noise level of a conventional 4.6 kΩ resistor. Typical current noise spectra of the studied p-GaAs HIWIP FIR detector at 4.2 K for various forward bias values are presented in Fig. 20. Similar noise behaviour was observed under reverse bias conditions. Also observed is the symmetry in dark current noise under forward and reverse biases due to the symmetric current-voltage (I–V) characteristics in HIWIP detectors. All the spectra display 1/f noise dependence at frequencies f below 1 kHz and are independent of frequency at higher values. The observed current noise spectra result from 1/f flicker noise and shot noise spectra. Absence of Lorentzian type noise in the noise spectra indicates that the current noise power density can be written as

$$S_i(f) = C^I \frac{I_d^\alpha}{f^\beta} + C^{II} \qquad (36)$$

where C^I is the amplitude of the flicker 1/f noise, and $C^{II} = 4q\, I_d g$ denotes the shot noise spectrum, as in QWIPs [47].

At low frequencies ($f \leq 1$kHz), the value of β is found to vary from 1.0 to 1.2 and no simple relationship was found between β and bias. In order to understand the origin of the 1/f noise, a plot of 1/f noise power density S_i as a function of dark current I_d at frequencies of 10, 100, and 500 Hz is measured and shown in Fig. 21. It is found that the 1/f noise power density is proportional to I_d^α with an α value of 2.05 ~ 2.10. This type of behavior indicates that the origin of the 1/f noise could be interpreted in terms of

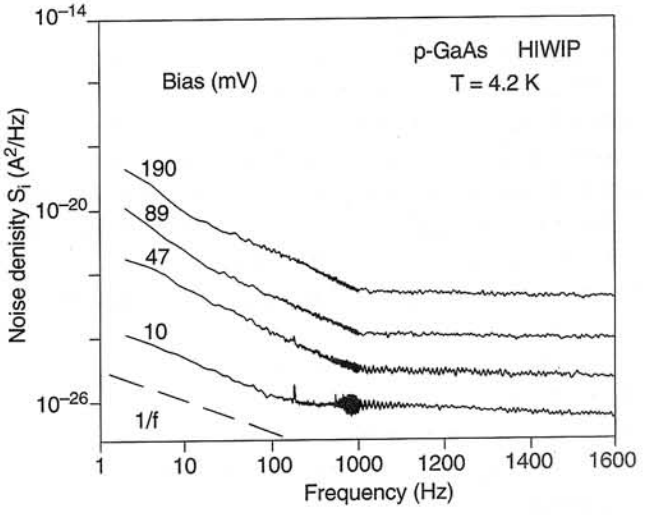

Fig. 20. Measured dark current noise spectra of p-GaAs HIWIP far-infrared detector at 4.2 K for various forward biases. The dashed line represents the 1/f dependence of the noise power density S_i.

a random fluctuation in the occupancy of the interface trap centers which can lead to generation-recombination (G–R) 1/f noise [78]. Two representative models of the 1/f noise have been proposed [79,80]. One model, the number fluctuation theory [79], is based on the slow fluctuations in the total number of carriers taking part in hopping conduction, resulting in the f^{-1} frequency and I_d^2 dark current dependences of the noise power density given by the well-known Hooge formula [81]. The other model [80] predicts a linear dependence of S_i on I_d. The free carrier absorption and internal photoemission in HIWIP detectors lead to carrier number fluctuations, which would result in current fluctuations in the external circuit when a net current flows through the detector. This kind of noise is related to the presence of interface localized states [78], which is in good agreement with the results from the detector response spectra, where one remarkably reproduciable spike response was observed and attributed to the localized nature of interface states.

The origin of the interface states, which normally have a sheet density of $10^{10} \sim 10^{12}$ cm^{-2}, can be the dangling bonds in the interfaces, Coulomb potential of charged ions, and impurities near interfaces [82,83]. If the G–R current noise is generated mostly by interface states near the Fermi level, the interface states can be estimated from the noise power density S_i by the following equation [78]

$$S_i(f) = \frac{C}{A_0} \frac{I_d^2}{f N_{is}} \tag{37}$$

where C is a constant which in practice ≈ 0.1, $A_0 = 1.6\times10^{-3}$ cm^2, and N_{is} is the interface state density.

Since the energy distribution of interface states is determined by the Fermi level, the density of interface states should change exponentially with the Fermi level, providing an independent confirmation. Under different biases, the position of the Fermi level at the interfaces with respect to the barrier is determined by the barrier lowering $\Delta\Phi$. Figure 22 shows the density of interface states obtained from Eq. (37) as a function of barrier lowering $\Delta\Phi$ calculated from Eq. (14). Accordingly N_{is} was found to increase exponentially with the barrier lowering, which can be well fitted (the solid line in Fig. 20) by an empirical state-density distribution

$$N_{is} = N_{is0} \exp\left(\frac{\Delta\phi}{E_i}\right) \tag{38}$$

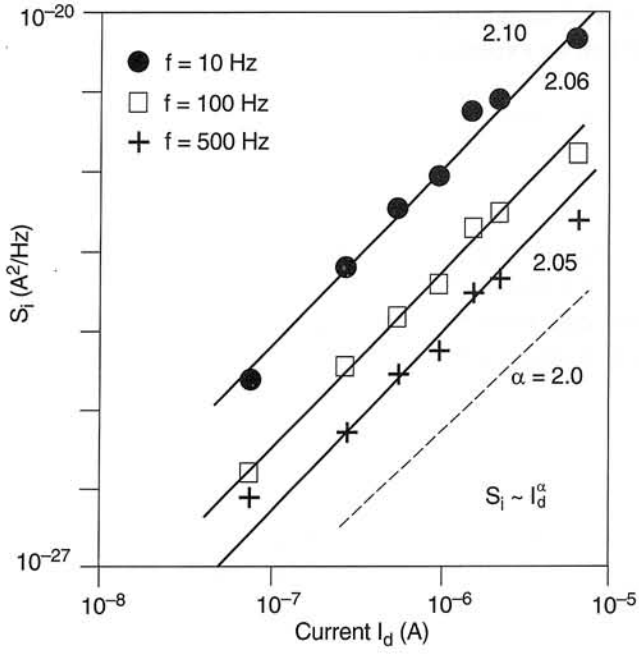

Fig. 21. 1/f noise power density S_i as a function of the dark current I_d at frequencies of 10, 100, 500 Hz. The dashed line represents the I_d^2 dependence of the noise power density S_i.

with $N_{is0} = 3.5\times10^{11}$ cm^{-2} and $E_i = 1.75$ meV. The estimated N_{is} is in the order of $10^{10} \sim 10^{11}$ cm^{-2}, a value which compared favorably with the density of interface states (2.5×10^{11} cm^{-2}) reported for MBE grown Be-doped p-type GaAs [84].

The capacitance and conductance of the detector were also measured at 4.2 K with the help of a Hewlett-Packard multifrequency LCR meter (4284 A). The interface state density was calculated and integrated as a function of bias from the low frequency (10 KHz) capacitance data with the relation $N_{is} = \int C_{is}/q^2A_0$, where C_{is} was the interface state capacitance calculated from an equivalent circuit of the detector, which is similar to the GaAs/AlGaAs QWIPs [85]. Shown in the inset of Fig. 22 is the interface state density obtained via capacitance-voltage (C-V) measurements, comparing with the results from the noise measurements. The interface state results from C–V measurements roughly agree with the order of 10^{11} cm^{-2} and show the same bias dependent behaviour as the noise measurements. The C–V measurements are much noisier at frequencies below 10 KHz. However, the estimation from noise measurements is only valid below 1 KHz. This difference in frequency may have resulted in the deviation in estimating the interface states.

The noise measurements also provide a means for gain determination [47]. For frequencies above 1 kHz,

 © 1999 COSiW SEP, Warsaw

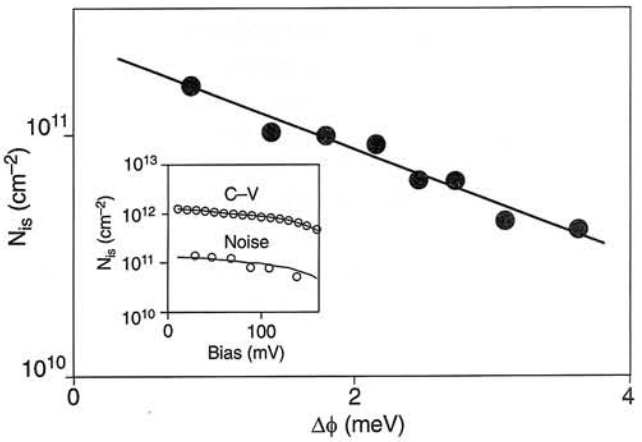

Fig. 22. Interface state density N_{is} as a function of barrier lowering $\Delta\phi$ due to the image force effect, which changes the position of the Fermi level at the interfaces with respect to the barrier. The solid line is a curve fitted to Eq. (38) with fitting parameters of $N_{is0} = 3.5\times10^{11}$ cm^{-2}, and $E_i = 1.75$ meV. Shown in the inset is the interface state density obtained via capacitance-voltage (C–V) measurements and noise measurements.

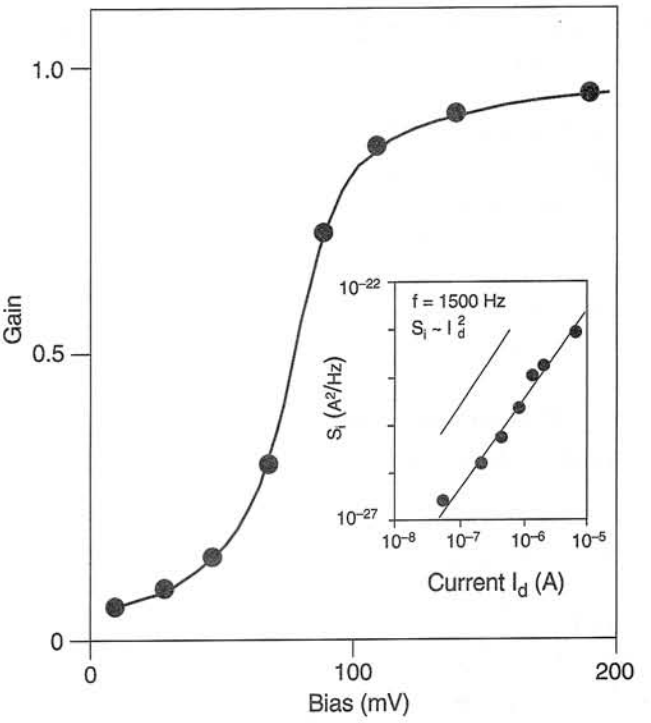

Fig. 23. Experimentally determined gain g vs forward bias for the p-GaAs HIWIP detector at 4.2 K. The smooth curve is drawn through the measured data. The inset shows the shot noise power density S_i as a function of the dark current I_d at a frequency of 1.5 kHz.

the noise was independent of frequency and was dominated by shot noise. The gain g can be obtained using the current shot noise expression [C^{II} in Eq. (36)]. Combining S_i and I_d allows the experimental determination of g as shown in Fig. 23, where the smooth curve is drawn through the experimental points. For this HIWIP detector, the determined gain increases rapidly with bias at low voltages, and gradually saturates (near the bias with the highest detectivity). This behaviour is similar to the case of QWIPs [47]. The highest value of g is ~0.95 at a bias corresponding to the highest responsivity. This value of gain is in good agreement with the previous estimation of 0.984, by combining the experimental responsivity and quantum efficiency.

Furthermore, using the optical gain equation we have derived for HIWIP detectors: $g = 1 - P_c$, the shot noise power density can be rewritten, if we ignore the difference between noise gain and optical gain, as

$$S_i = 4qI_d(1-P_c) \tag{39}$$

The dark current in HIWIP detector is also related to P_c

$$I_d = qGA_0W_e(1-P_c) \tag{40}$$

where W_e is the thickness of a single emitter layer. The thermal generation rate G (per unit volume) of a single emitter layer provides carriers for internal photoemission and have a probability $(1 - P_c)$ to escape. Substituting Eq. (40) into Eq. (39) gives

$$S_i = \frac{4I_d^2}{GA_0W_e} \tag{41}$$

which shows the shot noise power density is also proportional to I_d^2, similar to the 1/f noise. This can be clearly seen in the inset of Fig. 23, where the shot noise S_i is displayed as a function of dark current at a frequency of 1.5 kHz. Similar results have been obtained in GaAs/AlGaAs QWIPs [86]. Furthermore, equaling Eqs. (37) and (41) yields for the corner frequency f_c

$$f_c = \frac{CGW_e}{4N_{is}} \tag{42}$$

The fact that in Fig. 20 the corner frequency increases with increasing bias suggests indeed that N_{is} is reducing with bias (provided G is constant). However, the corner frequency variation with bias can not be determined accurately (see Fig. 20).

The measured shot noise data can be used to directly estimate the noise equivalent power (NEP) in the p-GaAs HIWIP FIR detector via NEP = $\sqrt{S_i}/R$, where R is the responsivity. At a bias of 89 mV, the measured shot noise S_i is 8.3×10^{-25} A^2/Hz, and the responsivity of the detector is 2.12 A/W. This yields a NEP of 4.3×10^{-13} $W/\sqrt{Hz}$ (detectivity D^* of 6.0×10^{10} $cm\sqrt{Hz}/W$), also in good agreement with the previous optical estimation D^* of 5.9×10^{10} $cm\sqrt{Hz}/W$ at a bias of 83 mV.

5.7. Comparison with Ge:Ga photoconductor

These experimental results are comparable to the performance of the best Ge:Ga photoconductor detector operated at 3.0 K [27], with responsivity ~5.2 A/W, and detector quantum efficiency ~7.7%. The responsivity (quantum efficiency) of the HIWIP could be further improved by employing optimum parameters and an optical cavity. In addition to this, the present GaAs HIWIP detectors have potential advantages including

(i) the easy tunability of response and cutoff wavelength by the emitter layer concentration and the applied bias, and the enhancement of response bandwidth and multi-wavelength detection by employing different concentration in multilayers,

(ii) the mature GaAs growth technology [high uniformity and well controlled MBE growth with high yield (thus low cost)], and monolithic integration technology for large arrays (128×128 or larger). In comparison, there are many technological challenges for building large format arrays in germanium [27]. However, the HIWIP detectors are low impedance electrical devices (dark resistance ~60 kΩ at 4.2 K compared to that of $\geq10^{10}$ Ω in Ge:Ga at 3.0 K [27], resulting in relatively high dark current. Since the previous p^+-n-n^+ samples show extremely low dark current [26], approaching the measurement limits, one should be able to reduce the dark current significantly by embedding the HIWIP detectors in a p-n junction.

6. Summary and discussion

It is shown that homojunction internal photoemission (HIP) detectors can be classified into three types in terms of the doping concentration in the emitter layer: type I ($N_a < N_c$), type II ($N_c < N_a < N_0$), and type III ($N_a > N_0$). Their photoresponse mechanisms have been distinguished and compared. In principle, λ_c can be tailored by changing the doping concentration. An analytic expression from the high-density theory has been used to obtain the λ_c vs N_a relationship in type II HIWIP FIR detectors, where an analytic model has been introduced to describe carrier photoemission processes. This model includes photoexcitation due to free carrier absorption, internal photoemission, and interfacial barrier collection due to the image force effect. For GaAs p^+-i structures, the effects of doping concentration, emitter layer thickness, applied bias voltage (electric field), on photoresponse performance (spectral response and quantum efficiency), have been calculated and shown high performance Si or GaAs FIR detectors ($\lambda_c > 40$ μm) can be achieved.

The HIWIP concept using MBE grown GaAs p^+-i multilayer structures have been demonstrated experimentally. A theoretical and experimental study of the performance of p-GaAs HIWIP FIR detectors as a function of emitter layer concentration was carried out. Thermionic field emission was found to be a major source of dark current. By comparison with the theory, the leakage current and defect induced current have been identified. A reasonable agreement was found between the experimental λ_c and the high density theory. A linear regression relationship between the absorption coefficient and the hole concentration has been obtained and employed to calculate the photon absorption probability, which is found to follow the detector responsivity well.

The HIWIP detector characteristics, such as responsivity, quantum efficiency, bias effect, detectivity, uniformity, crosstalk, photoconductive gain, response time, and noise, have been investigated in detail in a high performance p-GaAs HIWIP FIR detector, which shows a responsivity of 3.10 ±0.05 A/W, a η of 12.5% and a detectivity D^* of 5.9×10^{10} $cm\sqrt{Hz}/W$ at 4.2 K, for λ_c from 80 to 100 μm. The preliminary radiation exposure test of the HIWIP detectors shows they are radiation hard. A comparison with Ge:Ga photoconductive detectors suggests that a similar or even better performance may be obtainable. Preliminary results obtained are promising and show that p-GaAs HIWIP detectors have great potential to become a strong competitor in FIR applications.

It is clear that higher performance and longer λ_c (~200 μm) p-GaAs HIWIP FIR detectors can be obtained with the emitter layer concentration in the order of 10^{19} cm^{-3}. Also experimentally demonstrated was the Si type I HIP FIR detectors using MBE grown Si p^+-i multilayer structures [87]. Further work

 © 1999 COSiW SEP, Warsaw

is under way to design and fabricate high doping concentration type II Si HIWIP FIR detectors and longer λ_c (~200 μm) GaAs detectors. It is also possible to design detectors with wider wavelength ranges or to have multicolor detectors by changing the adjacent emitter layer doping concentrations.

The surface or interface defect states can influence both the dark current and the responsivity spectrum. Some passivation procedures may be necessary to overcome this problem. Further performance enhancement could be obtained by using an optical cavity or an antireflection coating (especially for shorter wavelength structures) to increase the internal photoemission efficiency. The response of detectors shows a broad spectrum (20–70 μm), the responsivity can further be enhanced by using filters to narrow the incident bandwidth [20]. Reducing the dark current leakage, the NEP values of the p-GaAs HIWIP FIR detectors could reach about 10^{-14} (or even 10^{-15}) W/√Hz by using high quality material and guard rings to suppress the edge leakage. Embedding the HIWIP detectors in a p-n junction will give rise to a similar situation that could lead to much lower dark current and NEP.

Acknowledgments

This work was supported in part by the National Aeronautics and Space Administration under contract No. NAG 5–4950. The authors would like to acknowledge Dr H.X. Yuan for help in early stages, Dr W.J. Schaff at Cornell University for his sample growth, Dr H.C. Liu, M. Buchanan, P. Chow-Chong, P. Marshall, and S.J. Rolfe at NRC, Canada, for sample fabrication and SIMS measurements, and Dr S.G. Matsik and Mr S.K. Gamage at GSU for their technical help.

References

1. M.W. Werner and M. Bothwell, "The SIRTF Mission", presented at Infrared/Submilimeter Astronomy Symposium, COSPAR/World Space Congress, published in *Advances in Space Research*, 1992.
2. E.E. Haller, M.R. Hueschen, and P.L. Richards, "Ge:Ga photoconductors in low infrared backgrounds", *Appl. Phys. Lett.* **34**, 495 (1979).
3. D.M. Watson and J.E. Huffman, "Germanium blocked-impurity-band far-infrared detectors", *Appl. Phys. Lett.* **52**, 1602 (1988).
4. I.C. Wu, J.W. Beeman, P.N. Luke, W.L. Hansen, and E.E. Haller, "Ion-implanted extrinsic Ge photodetectors with extended cutoff wavelength," *Appl. Phys. Lett.* **58**, 1431 (1991).
5. R. Katterloher, L. Barl, J. Beeman, E. Czech, D. Engemann, O. Frenzl, N. Haegal, E.E. Haller, Th. Henning, L. Hermans, G. Jakob, M. Konuma, and G. Pilbratt: "The 4×32 FIRGA array a pacesetter for a 52×32 element gallium arsenide focal plane array", *Proc. SPIE* **3354**, 57 (1998).
6. J.W. Beeman and E.E. Haller, "Ge:Ga photoconductor arrays: Design considerations and quantitative analysis of prototype single pixels", *Infrared Phys. Technol.* **35**, 827 (1994).
7. N. Sclar, "Properties of doped silicon and germanium infrared detectors", *Progress in Quantum Electronics*, Vol. 9, pp. 149-257 (1984).
8. F.D. Shepherd, V.E. Vickers and A.C. Yang, "Schottky barrier photodiode with degenerate semiconductor active region", U.S. Patent No. 3,603,847, (Sept. 1971).
9. F.D. Shepherd, "Infrared internal emission detectors", *Proc. SPIE* **1735**, 250 (1992).
10. W.F. Kosonocky, "State-of-art in Schottky-barrier IR image sensors", *Proc. SPIE* **1685**, 2 (1992).
11. T.L. Lin and J. Maserjian, "Novel $Si_{1-x}Ge_x$/Si heterojunction internal photoemission long--wavelength infrared detectors", *Appl. Phys. Lett.* **57**, 1422 (1990).
12. B.Y. Tsaur, C.K. Chen, and S.A. Marino, "Long-wavelength Ge_xSi_{1-x}/Si heterojunction infrared detectors and focal plane arrays", *Proc. SPIE* **1540**, 580 (1991).
13. S. Tohyama N. Teranishi, K. Kunoma, M. Nishimura, K. Arai, and E. Oda, "A new concept silicon homojunction infrared sensor", *IEDM Technical Digest IEEE*, pp. 82–85, 1988.
14. V.L. Dalal, "Simple model for internal photoemission", *J. Appl. Phys.* **42**, 2274 (1971).
15. V.E. Vickers, "Model of Schottky barrier hot--electron-mode photodetection", *Appl. Opt.* **10**, 2190 (1971).
16. J.M. Mooney and J. Silverman, "The theory of hot-electron photoemission in Schottky-barrier IR detectors", *IEEE Trans. Electron Devices* **ED-32**, 33 (1985).
17. J.M. Mooney, "The dependence of the Schottky emission coefficient on reverse bias", *J. Appl. Phys.* **65**, 2869 (1989).

18. D E. Mercer and C.R. Helms, "A diffusion model for the internal photoresponse of PtSi/p-Si Schottky barrier diodes", *J. Appl. Phys.* **65**, 5035 (1989).
19. D.D. Coon, R.P. Devaty, A.G.U. Perera, and R.E. Sherriff, "Interfacial work functions and extrinsic silicon infrared photocathodes", *Appl. Phys. Lett.* **55**, 1738 (1989).
20. A.G.U. Perera, R.E. Sherriff, M.H. Francombe, and R.P. Devaty, "Far infrared photoelectric thresholds of extrinsic semiconductor photocathodes", *Appl. Phys. Lett.* **60**, 3168 (1992).
21. A.G.U. Perera, J.W. Choe, M.H. Francombe, R.E. Sherriff, and R.P. Devaty, "Far infrared detection with a Si p-i interface and multilayer structures", *Superlattices and Microstructures* **14**, 123 (1993).
22. H.C. Liu, J.P. Noel, Lujian Li, M. Buchanan, and J.G. Simmons, "Novel infrared detector concept utilizing controlled epitaxial doping profiles", *Appl. Phys. Lett.* **60**, 3298 (1992).
23. A.G.U. Perera, H.X. Yuan, and M.H. Francombe, "Homojunction internal photoemission far-infrared detectors: Photoresponse performance analysis", *J. Appl. Phys.* **77**, 915 (1995).
24. N.M. Haegel, "Space-charge behavior near implanted contacts on infrared detectors", *J. Appl. Phys.* **64**, 2153 (1988).
25. H.X. Yuan and A.G.U. Perera, "Dark current analysis of Si homojunction interfacial workfunction internal photoemission far-infrared detectors", *Appl. Phys. Lett.* **66**, 2262 (1995).
26. A.G.U. Perera, "Physics and novel device applications in semiconductor homojunctions", in *Physics of Thin Films*, Vol. 21, pp. 1-75, edited by M.H. Francombe and J.L. Vossen, Academic Press, New York, 1995.
27. E.E. Haller, "Advanced far-infrared detectors", *Infrared Phys.* **35**, 127 (1994).
28. D.M. Watson, M.T. Guptill, J.E. Huffman, T.N. Krabach, S.N. Raines, and S. Satyapal, "Germanium blocked-impurity-band detector arrays: Unpassivated devices with bulk substrates", *J. Appl. Phys.* **74**, 4199 (1993).
29. E.S. Harmon, M.R. Melloch, and M.S. Lundstrom, "Effective band-gap shrinkage in GaAs", *Appl. Phys. Lett.* **64**, 502 (1994).
30. J.S. Escher, "NEA semiconductor photoemitters" in *Semiconductors and Semimetals*, Vol. 15, edited by R.K. Willardson and A.C. Beer, Academic Press, New York, 1981.
31. S.C. Jain, R.P. Mertens, and R.J. Van Overstraeten, "Bandgap narrowing and its effects on the properties of moderately and heavily doped germanium and silicon", in *Advances in Electronics and Electron Physics*, Vol. 82, edited by P.W. Hawkes, Academic Press, 1991.
32. M.D. Petroff and M.G. Stapelbroek, U.S. Patent No. 4,568,960, (Feb. 4, 1986).
33. F. Szmulowicz and F.L. Madarsz, "Blocked impurity band detectors – an analytical model: Figures of merit", *J. Appl. Phys.* **62**, 2533 (1987).
34. S.C. Jain and D.J. Roulston, "A simple expression for band gap narrowing (BGN) in heavily doped Si, Ge, GaAs, and Ge_xSi_{1-x} strained layers", *Solid State Electron.* **34**, 453 (1991).
35. G.D. Mahan, "Energy gap in Si and Ge: impurity dependence", *J. Appl. Phys.* **51**, 2634 (1980).
36. N.F. Mott, *Metal-Insulator Transitions*, Barnes and Noble, New York, 1974.
37. M.L. Huberman, A. Ksendzov, A. Larsson, R. Terhune, and J. Maserjian, "Optical absorption by free holes in heavily doped GaAs", *Phys. Rev.* **B44**, 1128 (1991).
38. W.Z. Shen, A.G.U. Perera, S.K. Gamage, H.X. Yuan, H.C. Liu, M. Buchanan, and W.J. Schaff, "A spectroscopic study of GaAs homojunction internal photoemission for infrared detectors", *Infrared Phys. Technol.* **38**, 133 (1997).
39. C.K. Chen, B.Y. Tsaur, and M.C. Finn, "Infrared absorption of Ir and IrSi thin films on Si substrates", *Appl. Phys. Lett.* **54**, 310 (1989).
40. T.L. Lin, J.S. Park, S.D. Gunapala, E.W. Jones, and H.M. Del Castillo, "Heterojunction internal photoemission $Si_{0.7}Ge_{0.3}$/Si infrared detector", *Opt. Eng.* **33**, 716 (1994).
41. O.S. Heavens, "Optical properties of thin solid films", in *Physics of Thin Films* Ch. 4, Dover Publications, New York, 1965.
42. A.G.U. Perera, W.Z. Shen, W. Mallard, K.L. Wang, and M. Tanner, "Far infrared free hole absorption in epitaxial silicon films for homojunction far-infrared detectors", *Appl. Phys. Lett.* **71**, 515 (1997).
43. D.K. Schroder, R.N. Thomas, and J.C. Swartz, "Free carrier absorption in silicon", *IEEE Transactions on Electron Devices* **ED-25**, 254 (1978).
44. R. Williams, "Injection by internal photoemission" in *Semiconductors and Semimetals*, Vol. 6, edited by R.K. Willardson and A.C. Beer, Academic Press, New York, 1970.

 © 1999 COSiW SEP, Warsaw

45. C.N. Berglund and R.J. Powell, "Photoinjection into SiO_2: Electron scattering in the image force potential well", *Appl. Phys.* **42**, 573 (1971).
46. S.M. Sze, *Physics of Semiconductor Devices* (2nd edition), John Wiley&Sons, New York, 1981.
47. B.F. Levine, "Quantum well infrared photodetectors", *J. Appl. Phys.* **74**, R1 (1993).
48. A.G.U. Perera, H.X. Yuan, S.K. Gamage, W.Z. Shen, M.H. Francombe, H.C. Liu, M. Buchanan, W.J. Schaff, "GaAs multilayer p^+-i homojunction far-infrared detectors", *J. Appl. Phys.* **81**, 3316 (1997).
49. J.S. Park, T.L. Lin, E.W. Jones, H.M. Del Castillo, and S.D. Gunapala, "Long-wavelength stacked SiGe/Si heterojunction internal photoemission infrared detectors using multiple SiGe/Si layers", *Appl. Phys. Lett.* **64**, 2370 (1994).
50. W.Z. Shen, A.G.U. Perera, M.H. Francombe, H.C. Liu, M. Buchanan, W.J. Schaff, "Effect of emitter layer concentration on the performance of GaAs p^+-i homojunction far-infrared detectors: A comparison of theory and experiment", *IEEE Trans. Electron Devices* **45**, 1671 (1998).
51. H.X. Yuan and A.G.U. Perera, "Effect of i layer parameters on the performance of Si n^+-i-n^+ homojunction far-infrared detectors", *IEEE Trans. Electron Devices* **44**, 2180 (1997).
52. H.X. Yuan and A.G.U. Perera, "Space-charge--limited conduction in Si n^+-i-n^+ homojunction far-infrared detectors", *J. Appl. Phys.* **79**, 4418 (1996).
53. R.E. DeWames, G.M. Williams, J.G. Pasko, and A.H.B. Vanderwyck, *J. Crystal Growth* **86**, 849 (1988).
54. G.M. Williams, R.E. De Wames, C.W. Farley and R.J. Anderson, "Excess tunnel currents in AlGaAs/GaAs multiple quantum well infrared detectors", *Appl. Phys. Lett.* **60**, 1324 (1992).
55. K. Vaccaro, A. Davis, H.M. Dauplaise, S.M. Spaziani, E.A. Martin and J.P. Lorenzo, "Cadmium sulfide surface stabilization for InP-based optoelectronic devices", *Journal of Electronic Materials* **25**, 603 (1996).
56. F.J. Low, "Low-temperature germanium bolometer", *J. Opt. Soc. America* **51**, 1300 (1961).
57. H.C. Liu, L.J. Li, J.M. Baribeau, M. Buchanan, and J.G. Simmons, "Long wavelength infrared photocurrent study of Si-SiGe heterostructures", *J. Appl. Phys.* **71**, 2039 (1992).
58. E.D. Palik and R.T. Holm, "Optical characterisation of semiconductors" in *Nondestructive Evaluation of Semiconductor Material and Devices*, edited by J.N. Zemel, Plenum Press, New York, 1979.
59. R.C. Newman, "Local vibrational mode spectroscopy of defects in III/V compounds" in *Semiconductors and Semimetals*, Vol. 38, Ch. 4, Academic Press, San Diego, 1993.
60. W.Z. Shen, A.G.U. Perera, H.C. Liu, M. Buchanan, and W.J. Schaff, "Bias effects in high performance GaAs homojunction far-infrared detectors", *Appl. Phys. Lett.* **71**, 2677 (1997).
61. J. Maserjian, "Long-wave infrared (LWIR) detectors based on III–V materials", *Proc. SPIE* **1540**, 127 (1991).
62. R.F. Lcheny and J. Shah, *Solid State Electronics* **21**, 167 (1978).
63. S.B. Stetson, D.B. Reynolds, M.G. Stapelbroek, and R.L. Stermer, "Design and performance of block-impurity-band detector focal plane arrays", *Proc. SPIE* **686**, 48 (1986).
64. G. Hasnain, B.F. Levine, S. Gunapala, and N. Chand, "Large photoconductive gain in quantum well infrared photodetectors", *Appl. Phys. Lett.* **57**, 608 (1990).
65. H.C. Liu, "Photoconductive gain mechanism of quantum-well intersubband infrared detectors", *Appl. Phys. Lett.* **60**, 1507 (1992).
66. K.K. Choi, "Generalized relationship between gain, noise, and capture probability of quantum well infrared photodetectors", *Appl. Phys. Lett.* **65**, 1266 (1994).
67. W.Z. Shen and A.G.U. Perera, "Photoconductive generation mechanism and gain in internal photoemission detectors", *J. Appl. Phys.* **83**, 3923 (1998).
68. J.S. Park, T.L. Lin, E.W. Jones, H.M. Del Castillo, T. George, and S.D. Gunapala, *Proc. SPIE* **2020**, 12 (1993).
69. L.C. West and S.J. Eglash, "First observation of an extremely large-dipole infrared transition within the conduction band of a GaAs quantum well", *Appl. Phys. Lett.* **46**, 1156 (1985).
70. Y. Marfaing, *Handbook on Semiconductors*, Vol. 2, North Holland Publication, 1980.
71. R.A. Suris and V.A. Fedirko, "Heating photoconductivity in a semiconductor with a superlattice", *Sov. Phys. Semicond.* **12**, 629 (1978).
72. S. Barbieri, F. Mango, F. Beltram, M. Lazzarino, and L. Sorba, "Hot-electron multiquantum well microwave detector operating at room temperature", *Appl. Phys. Lett.* **67**, 250 (1995).
73. E.R. Brown, K.A. McIntosh, F.W. Smith, and M.J. Manfra, "Coherent detection with a GaAs/

AlGaAs multiple quantum well structure", *Appl. Phys. Lett.* **62**, 1513 (1993).

74. H.C. Liu, J. Li, E.R. Brown, K.A. McIntosh, K.B. Nichols, and M.J. Manfra, "Quantum well intersubband heterodyne infrared detection up to 82 GHz", *Appl. Phys. Lett.* **67**, 1594 (1995).
75. W.Z. Shen and A.G.U. Perera, "Photoconductivity in homojunction internal photoemission far-infrared detectors", *Infrared. Phys. Technol.* **39**, 329 (1998).
76. K. Seeger, *Semiconductor Physics* (fifth edition), Ch. 6, Springer-Verlag, 1991.
77. W.Z. Shen and A.G.U. Perera, "Low frequency noise and interface states in GaAs homojunction far-infrared detectors", *IEEE Trans. Electron Devices* **46**, 811 (1999).
78. O. Jantsch, "Flicker (1/f) noise generated by a random walk of electrons in interfaces", *IEEE Trans. Electron Devices* **ED-34**, 1100 (1987).
79. B.I. Shklovskii, "Theory of 1/f noise for hopping conduction", *Solid State Commun.* **33**, 273 (1980).
80. M.Y. Luo, G. Bosman, A. Van der Ziel, and L.L. Hench, "Theory and experiments of 1/f noise in Schottky-barrier diodes operating in the thermionic-emission mode", *IEEE Trans. Electron Devices* **ED-35**, 1351 (1988).
81. F.N. Hooge, "1/f noise no surface effect", *Phys. Lett.* **A 29**, 139 (1969).
82. L. Vadasz and A.S. Grove, *IEEE Trans. Electron Devices* **ED-13**, 863 (1966).
83. M.M. Atella, E. Tannenbaum and E.J. Scheibner, *J. Bell Syst. Tech.* **30**, 749 (1959).
84. J. Qiu, Q.D. Qian, R.L. Gunshor, M. Kobayashi, D.R. Menke, D. Li, and N. Otsuka, "Influence of GaAs surface stoichiometry on the interface state density of as-grown epitaxial ZnSe/ epitaxial GaAs heterostructures", *Appl. Phys. Lett.* **56**, 1272 (1990).
85. A.G.U. Perera, V.G. Silvestrov, S.G. Matsik, H.C. Liu, M. Buchanan, Z.R. Wasilewski, and M. Ershov, "Nonuniform vertical transport and relaxation in quantum well infrared detectors", *J. Appl. Phys.* **83**, 991 (1998).
86. D. Wang, G. Bosman, and S.S. Li, "On the dark current noise of quantum well infrared photodetectors", *Appl. Phys. Lett.* **65**, 183 (1994).
87. A.G.U. Perera, W.Z. Shen, H.C. Liu, M. Buchanan, M.O. Tanner, and K.L. Wang, "Demonstration of Si homojunction far-infrared detectors", *Appl. Phys. Lett.* **72**, 2307 (1998).

 © 1999 COSiW SEP, Warsaw